Version 2.0 (accepted): June 24, 1999

Coronal heating by resonant absorption: the effects of chromospheric coupling

A.J.C. Beliën[1], P.C.H. Martens[2]
Solar System Division, ESA Space Science Department at Goddard Space Flight Center, Greenbelt, MD 20771; belien@rijnh.nl, martens@mithra.physics.montana.edu

and

R. Keppens
FOM-Institute for Plasma Physics 'Rijnhuizen',
P.O. Box 1207, 3430 BE, Nieuwegein,
The Netherlands

ABSTRACT

We present the first 2.5D numerical model calculations of the nonlinear wave dynamics and heating by resonant absorption in coronal loops with thermal structuring of the transition region and higher chromosphere. The numerical calculations were done with the Versatile Advection Code. The transition region can move freely and is transparent for mass motions from chromosphere to corona. The loops are excited at the chromospheric level by linearly polarized monochromatic Alfvén waves.

We find that the efficiency of resonant absorption can be much lower than in equivalent line-tied coronal loop models. The inefficiency is due to the fast rate at which slow magnetosonic waves are nonlinearly generated in the chromosphere and transition region. This leads to considerable transfer of energy from the Alfvén wave to the magnetosonic waves. Consequently, only a relatively small fraction of the Poynting flux that is injected into the loop system at the chromospheric level is available at the coronal level. Cavity leakage and detuning also have a negative impact on the efficiency but it is less than due to the nonlinear energy transfer. Inclusion of radiative and conductive losses improves the efficiency of resonant absorption.

While the efficiency of resonant absorption heating is low, our results indicate that heating by compression and dissipation of the slow magnetosonic waves and shocks can easily lead to a temperature rise of a few percent and for larger driver amplitudes even to a rise over ten percent. Hence, our results support the idea for indirect coronal

---

[1]Current address: FOM-Institute for Plasma Physics 'Rijnhuizen', P.O. Box 1207, 3430 BE Nieuwegein, The Netherlands

[2]Current address: Department of Physics, Montana State University, P.O. Box 173840, Bozeman, MT 59717-3840, USA

heating through the nonlinear generation of magnetosonic waves that has been put forward more than twenty years ago.

Furthermore, the large transition region and coronal density oscillations that are associated with the slow magnetosonic waves provide an explanation for some observed coronal and transition region loop EUV intensity variations.

Subject headings: MHD — waves — Sun: corona — Sun: transition region — Sun: chromosphere

1. Introduction

In the theory of wave heating mechanisms for the solar corona two concepts play a crucial role. The first is that of interference filters which allow for a large energy transfer via waves from the turbulent convection zone into the corona. The second one is the creation of short length scales so that dissipation of wave energy in the corona occurs at sufficiently short time scales that are necessary to balance the radiative and conductive losses.

These concepts stress different spatial dependencies, viz., the interference filter concept stresses variations along the magnetic field whereas the creation of small length scales stresses variations in the directions across the magnetic field. So far, most analytical and numerical studies have focussed on one or the other of these concepts only. High resolution numerical modeling and distributed memory execution allow us to investigate coronal loop dynamics with variations both along and across the magnetic field.

Once it was recognized that most of the hot emitting solar coronal plasma is confined in closed loop structures (Rossner, Tucker, & Vaiana 1978) and that extrapolation of force-free coronal magnetic fields from photospheric magnetograms revealed that these loops outline the magnetic field (e.g., Orrall 1981), coronal loop structures have played a key role in wave heating theories of the solar corona. Early on, it was recognized that due to the large atmospheric density stratification the loops act as interference filters for waves that are generated in the convection zone, travel upwards into the photosphere, chromosphere, transition region, and corona, and then return to the convection zone (Ionson 1978,1982; Hollweg 1981,1984a,b; Zhugzhda & Locans 1982). The interference filter gives rise to resonant transmission peaks in the frequency domain that allow the necessary large energy fluxes (10^2 Wm^{-2} for quiet Sun, 10^4 Wm^{-2} for active regions) to enter the loops. Besides depending on the Alfvén speed, the frequency of the peaks is determined by the length of the resonant cavity. This length can be thought of as the length of the axial magnetic field line running from the base of the transition region into the corona and back to the transition region. Since coronal loop lengths are highly varying, each loop will be sensitive to a different part of the power spectrum of wave perturbations available at its "footpoints".

Of the three types of MHD waves, Alfvén waves have received the most attention as the transport agent, being the natural waves to transport energy fluxes upwards along the magnetic field, and also the ones least susceptible to shock formation and dissipation in the lower solar atmosphere. For efficient dissipation of the energy carried by Alfvén waves, very small length scales have to be generated to strongly increase the dissipation that is otherwise very small due to the large coronal values of the viscous and magnetic Reynolds numbers. This is true for all coronal heating mechanisms based on Ohmic or viscous dissipation (Martens 1986; Browning 1991; Zirker 1993). For resonant absorption and phase mixing the variation of the Alfvén speed across the magnetic field plays a crucial role in the efficient creation of small length scales. The variation of the Alfvén speed makes that each magnetic flux surface in the corona has its own oscillation frequency $\omega = kv_{\mathrm{Alfvén}}$. For closed structures like coronal loops k is the wavenumber for standing waves in the coronal cavity. When an Alfvén wave that propagates into a coronal loop has a frequency that matches one of the local Alfvén frequencies, only the upward and downward propagating waves on the corresponding magnetic surface will be in phase with the incoming wave. Consequently, in a system without dissipation the amplitude on this surface growths unboundedly whereas on other surfaces the amplitudes remain bounded. This creates the small length scales necessary for efficient Ohmic dissipation. At the point where all injected wave energy is converted into Ohmic dissipation the system has reached a stationary state and the amplitude in the resonant layer does not grow anymore.

The properties of both resonant absorption and phase mixing were first studied as a possible means to heat tokamak plasmas (Tataronis & Grossmann 1973; Grossmann & Tataronis 1973; Tataronis 1975; Kappraff & Tataronis 1978).

For coronal loops the efficiency of resonant absorption of Alfvén waves has been rigorously studied both analytically and numerically (Davila 1987; Hollweg & Yang 1988; Grossmann & Smith 1988; Poedts, Goossens, & Kerner 1989; Poedts & Kerner 1992; Steinolfson & Davila 1993; Poedts, Beliën, & Goedbloed 1994; Ofman, Davila, & Steinolfson 1994a,1995; Halberstadt & Goedbloed 1995a,b; Goossens, Rudermann, & Hollweg 1995; Wright & Rickard 1995; Tirry, Berghmans, & Goossens 1997; Berghmans & Tirry 1997; Tirry & Berghmans 1997; Tirry & Poedts 1998). More recently, the effects of nonlinearity have been studied as well (Ruderman & Goossens 1993; Ofman, Davila, & Steinolfson 1994; Ofman & Davila 1995; Poedts & Boynton 1996; Poedts & Goedbloed 1997; Poedts, Tóth, Beliën, & Goedbloed 1997). All of these studies show that resonant absorption of Alfvén waves is a viable heating mechanism for solar coronal loops, provided that enough power is available in the Alfvén wave frequency ranges. Parker (1992) has argued that this is not the case since the involved frequencies are too high ($\gg 10$ mHz) and that at the photospheric level not enough power is available in this range. Goedbloed (1994) has countered this argument using a slip-stick argument where frequencies above 10 mHz are generated by motions with much lower frequencies just as a violin player uses slow motions of the bow to generate much higher sound frequencies. However, an equivalent mechanism in solar context has not been found yet.

The mentioned studies on resonant absorption have simplified the effects of the longitudinal variation by assuming fixed length loops which are anchored in an infinitely dense chromosphere/photosphere. This is inaccurate for the following reasons.

First, since the ratio of Alfvén speeds in the corona and underlying atmosphere is finite the quality of the cavity resonances will be finite as well and trapped waves will leak out of the cavity on a time scale $\tau_{\rm A}/|\ln R|$ where R is the reflection coefficient of the Alfvén speed discontinuity at the photosphere-corona interface and $\tau_{\rm A}$ is the time an Alfvén wave needs to propagate once along the loop (Berghmans & De Bruyne 1995). Considering that at the top of the photosphere the magnetic field is one to two orders of magnitude larger than in the corona and that the density is four to six orders larger, the ratio of Alfvén speeds will lie in the range 10–100. For ratios near 10 the reflection is approximately 0.8 and the time scale of leakage of the order of a few Alfvén crossing times only. Hence, leakage can severely hamper the build up of small length scales and large amplitudes and, thus, negatively affect the efficiency of these mechanisms.

Second, the transition region is a very dynamical medium that can easily be lifted over a few Megameters by the nonlinearly generated wave pressure, centrifugal forces, and magneto-acoustic shocks of upward propagating Alfvén waves (Hollweg 1982; Hollweg, Jackson, & Galloway 1982; Mariska & Hollweg 1985; Sterling & Hollweg 1988,1989; Sterling & Mariska 1990; Hollweg 1992; Cargill 1997; Kudoh & Shibata 1999). For loop lengths below 100 Mm this can lead to length changes of several percents. Consequently, tuning and detuning of the coronal cavity is expected to take place continuously and the build up of small length scales will certainly be affected.

The above arguments show the importance of the inclusion of the coupling of the coronal parts of loops with the transition region and chromosphere for understanding the wave dynamics and heating by resonant absorption. Therefore, in this paper we investigate numerically the nonlinear wave dynamics and properties of resonant absorption of such models and consider both variations across and along the magnetic field. We restrict ourselves to axisymmetric cylindrical loop models that are mono-periodically driven by linearly polarized Alfvénic perturbations in the chromosphere. Several runs with different driver amplitudes and frequencies, as well as different loop lengths, are studied. The major result will be that the efficiency of resonant absorption will be much lower than in equivalent line-tied loop systems and that compressional heating takes up a much more prominent role.

A direct consequence of taking into account the thermal structure of the transition region and chromosphere is that the effects of optically thin radiative losses and thermal conduction should be modeled as well since the associated time scales will compete with the MHD ones. First attempts to show the effects of radiative losses and thermal conduction on resonant absorption of Alfvén waves were carried out by Martens & Kuin (1983) and Offman, Klimchuk, & Davila (1998) using 1D models, in which the scaling laws for quiet coronal loops are used to update the frequency (Martens & Kuin) or the density (Offman et al). They find that the heating is concentrated in multiple resonant layers instead of a single one as found in previous model studies and that this is in better agreement with coronal observations. Therefore, we also compare a model simulation with and without radiative losses and thermal conduction. It turns out that the heating efficiency becomes better when those effects are taken into account.

This paper is organized as follows: In section 2, we describe the loop model that is used in our numerical calculations. In section 3, the results of several model runs are presented. Special attention is payed to the energetics and the nonlinear dynamics. We point out the relevance in explaining some loop brightenings in section 4. Finally, we discuss the results and draw our conclusions in section 5.

2. Numerical model

For the modeling of coronal loop structures we closely follow Beliën, Poedts, & Goedbloed (1997a,1997b). Longitudinal curvature of the coronal parts of the loops is neglected. Consequently, the loops are modeled as straight flux tubes of length L and with circular cross-section of radius $R(z)$ where z is the longitudinal coordinate of the exploited (r, θ, z) cylindrical coordinate system. The chromosphere is located at both ends of the flux tube. In this paper we consider a constant tube cross-section. Flux tube expansion is expected to have an impact on resonant absorption and on the nonlinear dynamics in general, because it will lower the ratio of Alfvén speeds between corona and chromosphere, and because all the basic MHD waves will become coupled by which excitation of linear polarized Alfvén waves will already lead to compressive motions in the linear regime. In future work, the effects of flux tube expansion will be studied.

2.1. Evolution equations

The evolution of the loops is studied using the MHD equations. The conservative form of the MHD equations for the evolution of the density ρ, the momentum $\rho\mathbf{v}$, the total energy e, and the magnetic field $\mathbf{B}$ is used:

$$\begin{aligned}
\frac{\partial \rho}{\partial t} + \nabla \cdot \rho\mathbf{v} &= 0, && \text{(1a)}\\
\frac{\partial \rho\mathbf{v}}{\partial t} + \nabla \cdot \left(\mathbf{v}\rho\mathbf{v} - \frac{\mathbf{BB}}{\mu_0}\right) + \nabla p_{\rm tot} &= \rho\mathbf{g}, && \text{(1b)}\\
\frac{\partial e}{\partial t} + \nabla \cdot \left((e + p_{\rm tot})\,\mathbf{v} - \frac{\mathbf{BB}}{\mu_0}\cdot\mathbf{v}\right) &= -\mathcal{L} - \nabla \cdot \eta\mathbf{J}\times\mathbf{B} + \mathbf{g}\cdot\rho\mathbf{v}, && \text{(1c)}\\
\frac{\partial \mathbf{B}}{\partial t} + \nabla \cdot (\mathbf{vB} - \mathbf{Bv}) &= -\nabla \times \eta\mathbf{J}. && \text{(1d)}
\end{aligned}$$

Here, the gas pressure, p, the total gas and magnetic pressure, $p_{\rm tot}$, and the current density, $\mathbf{J}$ are defined by

$$p = (\gamma - 1)\left(e - \frac{\rho\mathbf{v^2}}{2} - \frac{\mathbf{B}^2}{2\mu_0}\right), \qquad p_{\rm tot} = p + \frac{\mathbf{B}^2}{2\mu_0}, \qquad \mathbf{J} = \frac{1}{\mu_0}\nabla\times\mathbf{B}, \tag{1e}$$

and the gas pressure is related with the number density and temperature, T, through the ideal gas law

$$p = nkT, \qquad n = \frac{\rho}{\bar{m}}. \tag{1f}$$

In the above equations, η is the electrical resistivity, $\bar{m}$ is the averaged particle mass, γ is the ratio of specific heats, μ_0 is the permeability of vacuum, and k is the Boltzmann constant. For convenience, we fix the average particle mass to 0.6 times the proton mass (acceptable for a hydrogen/helium coronal plasma), the ratio of specific heats to 5/3, and assume a constant resistivity.

The terms on the right hand sides of Eqs. (1b)–(1d) represent sources. The only source appearing in the momentum equation (1b) comes from the gravitational force. The source term in the induction equation (1d) comes from the diffusion of the magnetic field. Finally, the first term in energy equation (1c) represents heat sources and sinks, the second term represents magnetic stresses due to slipping of the magnetic field through the plasma fluid, and the last one represents the work done by gravity. Note that the source $\mathcal{L} = 0$ for those simulations in which we neglect radiative losses and thermal conduction. Otherwise, the form of $\mathcal{L}$ is given by

$$\mathcal{L} = \nabla \cdot \mathbf{q} + \frac{n^2}{4} Q(T) - h(\mathbf{r}, \rho, T). \tag{1g}$$

The first term on the right hand side represents the thermal losses where $\mathbf{q} = -\boldsymbol{\kappa} \cdot \nabla T$ is the heat flux. For the thermal conduction tensor we take $\boldsymbol{\kappa} = \kappa_{||} \mathbf{e_B} \mathbf{e_B}$, where $\mathbf{e_B}$ is unit vector along the magnetic field. This form neglects the conduction perpendicular to the magnetic field, while $\kappa_{||}(T) = 1.8 \times 10^{-10} \Lambda^{-1} T^{2.5}$ $\mathrm{Wm^{-1}K^{-1}}$ following Braginskii (1965). The second term corresponds to the optically thin radiative losses. For $Q(T)$ the analytical fit by Rossner et al. (1978) of the semi-empirical calculations of the loss function by Raymond & Smith (1977) is used. The third term h is a heat source which sole purpose is to balance the losses in the initial state. We do not specify the nature of this heat source. Time dependence of h enters via the density and temperature dependence for which we will take a power law, viz., $h \propto \rho^2 T^{-1}$. This particular scaling has been chosen for our convenience and also to make sure that the loop is thermally stable. Note, however, that loop dynamics are sensitive to the specific density and temperature scaling of the heat source. It is outside the scope of this paper to investigate this sensitivity.

The gravitational acceleration is modeled as

$$\mathbf{g}(z) = -g_\odot \cos\left(\frac{\pi z}{L}\right) \mathbf{e}_z, \tag{2}$$

where $g_\odot$ takes on the solar surface value, viz., $g_\odot = 274$ $\mathrm{ms^{-2}}$. Equation (2) is the usual representation of the projection of the gravitational force along the magnetic field.

Using the loop radius, $a = 10^6$ m, the coronal temperature on axis, $T_{\mathrm{cor}} = 10^6$ K, and the coronal magnetic field strength on axis, $B_{\mathrm{cor}} = 25 \times 10^{-4}$ T, we make all variables dimensionless by the following transformations:

$$r \rightarrow \frac{r}{a}, \qquad z \rightarrow \frac{z}{a}, \qquad t \rightarrow \frac{t}{\tau_{\mathrm{s}}}, \qquad \eta \rightarrow \frac{\eta}{\mu_0 c_{\mathrm{s}} a}, \qquad g_\odot \rightarrow \frac{a g_\odot}{c_{\mathrm{s}}^2} \tag{3a}$$

$$\rho \rightarrow \frac{\mu_0 c_{\mathrm{s}}^2 \rho}{B_{\mathrm{cor}}^2}, \qquad e \rightarrow \frac{B_{\mathrm{cor}}^2 e}{\mu_0}, \qquad p \rightarrow \frac{B_{\mathrm{cor}}^2 p}{\mu_0}, \qquad p_{\mathrm{tot}} \rightarrow \frac{B_{\mathrm{cor}}^2 p_{\mathrm{tot}}}{\mu_0}, \qquad T \rightarrow \frac{T}{T_{\mathrm{cor}}}, \tag{3b}$$

$$\mathbf{v} \rightarrow \frac{\mathbf{v}}{c_{\mathrm{s}}}, \qquad \mathbf{B} \rightarrow \frac{\mathbf{B}}{B_{\mathrm{cor}}}, \qquad \mathbf{J} \rightarrow \frac{\mu_0 a \mathbf{J}}{B_{\mathrm{cor}}}. \tag{3c}$$

where $c_{\mathrm{s}} = \sqrt{kT_{\mathrm{cor}}/\bar{m}}$ is the coronal isothermal sound speed and $\tau_{\mathrm{s}} = a/c_{\mathrm{s}}$. The value of the dimensionless resistivity is fixed to 10^{-4} in our simulations. This corresponds to a Lundquist number $S \equiv \mu_0 c_{\mathrm{a}} L/\eta \approx 5 \times 10^4$.

2.2. Initial state

We consider an axisymmetric, two-dimensional magnetostatic equilibrium as our initial state. The magnetic field is twist free and predominantly directed along the loop axis. The length of the loop is specified as $L = 8\pi a$. The equilibrium is calculated by numerically solving the Grad-Shafranov equation for the longitudinal magnetic flux (e.g, Low 1975; Beliën et al. 1997a,b). For this purpose, a slightly adapted version of the cubic Hermite finite element code PARIS (Beliën et al. 1997b) is used. The adaptation amounts to a rearrangement of the profiles and parameters that can be specified freely. Those free profiles are the temperature and the chromospheric ratio of kinetic to magnetic pressure, β.

The temperature profile is normalized to T_{cor}. We assume that its spatial dependence is separable and that it takes the following form:

$$T(\psi, z) = \Theta(\psi)\Xi(z), \tag{4a}$$

$$\Theta(\psi) = 1 + \theta_1 \psi + \theta_2 \psi^2, \tag{4b}$$

$$\Xi(z) = \frac{1}{2}(1+\xi) + \frac{1}{2}(1-\xi)\tanh\left(\frac{z - z_{\mathrm{t}}}{w_{\mathrm{t}}}\right). \tag{4c}$$

Here, $\psi = \psi(r,z)$ is the normalized longitudinal magnetic flux $\psi \equiv \Psi(r,z)/\Psi(r = R)$. The parameter ξ is approximately the chromospheric ($z = 0$) to coronal ($z = L/2$) temperature ratio. The parameters z_{t} and w_{t} determine the position and width of the transition region, respectively.

The dimensionless gas pressure P is given by

$$P(\psi, z) = \tfrac{1}{2}\beta(\psi)\exp\left(-\int_0^z \frac{1}{H(\psi, z')} dz'\right), \tag{5a}$$

$$\beta(\psi) = \beta_{\mathrm{chr}}\left(1 + b_1\psi + b_2\psi^2\right), \tag{5b}$$

where H is the dimensionless pressure scale height $kT/(a\bar{m}g)$. Finally, $\beta_{\rm chr}$ is the chromospheric value of the plasma beta on axis. It is related to the coronal value by $\beta_{\rm cor} = \beta_{\rm chr} \exp\left(-\int_0^{L/2} H^{-1}(0,z)dz\right)$.

In Fig. 1, the spatial dependence of the density, pressure, and temperature is plotted for our reference initial state.

2.3. Numerical method

To solve the set of MHD equations (1a)–(1d) we use the Versatile Advection Code (VAC) (Tóth 1996; Tóth & Odstrčil 1996).

VAC offers a choice of various spatial and temporal discretizations, all second order accurate in time and space for smooth solutions. Since our simulations involve resonant layers and induced shock interactions, a low numerical diffusion and high robustness is desired. These aspects of the different algorithms are critically compared in Tóth & Odstrčil (1996). The results discussed below are obtained with the TVD method based on Roe's approximate Riemann solver (Roe 1981), which in our experience meets the requirements best. The validity of our results has been checked by control calculations making use of the FCT algorithm (Boris & Book 1973; Odstrčil 1990).

Since the source terms in Eqs. (1b)–(1d) are added explicitly, we ensure stability by additional CFL-limitations on the time step (resulting from the diffusion time of the heat conduction over one computational cell, the radiative loss time scale, etc.). To suppress the effects introduced by a non-zero divergence of the magnetic field Powell source terms are added (Powell 1994). These source terms guarantee that the errors will remain bounded and they are also responsible for the propagation of the errors as "div B" waves. However, the errors still remain and, therefore, every 250th time step a projection method is applied to the magnetic field that will make it divergence free again.

2.4. Boundary conditions

To complete our model radial and longitudinal boundary conditions have to be specified.

To conserve the total mass in the system, and also to avoid numerical instabilities that might lead to a fast draining of the loop, the normal components of the velocity are forced to zero, effectively creating reflective boundaries.

We allow the Alfvén wave to freely propagate out of the chromospheric end planes. This is achieved by a zero order extrapolation of the outgoing Alfvén wave characteristics. However, this zero order extrapolation does not create a completely free boundary. Tests show that some of the Alfvén wave energy is being reflected back, although less than a few percents.

At $z = 0$, the bottom of our chromospheric domain, mono-periodic Alfvén waves are launched by prescribing v_θ, viz.,

$$v_\theta = \begin{cases} 0 & 0.0 \le r/a < 0.3 \\ v_\mathrm{d} \left(\frac{10}{3}\right)^4 \left(\frac{r}{a} - 0.3\right)^2 \left(\frac{r}{a} - 0.9\right)^2 \sin\left(\frac{2\pi t}{P_\mathrm{d}}\right) & 0.3 \le r/a \le 0.9 \\ 0 & 0.9 < r/a \le 1.0 \end{cases} \tag{6}$$

where v_d is the maximum amplitude at $r = 0.6$ and P_d is the period of the excitation. We consider here a mono-periodic driver only in order to keep the complexity of the results down. In future work we intend to consider more realistic random broad band excitation spectra.

All other variables at the radial and longitudinal boundaries are treated as flow through variables.

3. Results

We have performed six simulations, specified in table 1. Runs 1, 2, and 3 are used to investigate the dependence on the driver amplitude v_d. Run 4 is identical in setup to run 3, but takes account of radiative and conductive losses. Run 5 differs from run 3 in driver period only. Run 6 is a control run without Alfvén resonance.

The minimum value of the driver amplitude is restricted by numerical considerations. The driver amplitude should not be less than approximately 5 km/s since the initial state will always give rise to some transients with maximum velocities up to a few km/s. If the driver amplitude is too small it becomes hard to distinguish between transients and driven effects. Our choice of amplitudes, however, is still reasonable. In granules velocities around 1 km/s are observed. Since the bottom of the chromosphere in our model ($z = 0$ and $z = L$) is at least a few thousand kilometers above the location of the granules in the photosphere/low chromosphere, the large density stratification makes that upward propagation of the granule velocities of 1 km/s by Alfvén waves easily lead to velocities of 3 to 10 km/s (take a density ratio of 10–100, a constant Alfvén speed, and assume that $\rho v^2 v_\mathrm{Alfvén}$ remains constant). The largest amplitude, $v_\mathrm{d} = 23.5$ km/s, is, therefore, likely to be less realistic but it will exhibit the nonlinear effects as seen in the smaller amplitude cases much better.

The different driver periods correspond, in the linear MHD limit, to local Alfvén resonances at $r \approx 0.7$ for $P_\mathrm{d} = 41.1$ s, and at $r \approx 0.55$ for $P_\mathrm{d} = 53.4$. Here the position of the resonant layers has been obtained by inspection. Exact values of the resonant positions could have been obtained by solving a set of two coupled ordinary differential equations that govern the slow and Alfvén continua, see, e.g., Beliën et al. (1997a). For the purpose of this paper, exact knowledge on the resonant position is not important. For run 6, with a driver period of $P_\mathrm{d} = 66.7$, inspection did not reveal the creation of a resonance layer. The corresponding driver frequency lies below the Alfvén continuum. This run has been included to investigate the difference between driving with frequencies that are located inside and outside the ideal MHD Alfvén continuum.

We typically run the simulations for a time corresponding to about 8 to 23 driving periods, which is sufficient to determine quantitative information on the evolution of coronal loop dynamics and on the heating efficiency.

3.1. Energetics

Before we quantitatively study the efficiency of the resonant absorption process, we focus on the evolution of the variation of the total (=gas + kinetic + magnetic) energy E, kinetic energy K, magnetic energy M, gravitational energy G, internal energy U, and the total Ohmic dissipation OD. The evolution of these quantities provides us with valuable information on the dynamics taking place in the loop structure. The differences in the evolution of the energetic quantities compared to known results for resonant absorption in line-tied loops are good indicators of the effects this chromospheric coupling has on the resonant absorption process and the loop dynamics in general.

The total, kinetic, magnetic, gravitational, and internal energy variations, and the total Ohmic dissipation are defined as follows:

$$E \equiv \langle e(\mathbf{r},t)\rangle - \langle e(\mathbf{r},0)\rangle\,, \tag{7a}$$

$$K \equiv \frac{1}{2}\left\langle \rho(\mathbf{r},t)\mathbf{v}^2(\mathbf{r},t)\right\rangle, \tag{7b}$$

$$M \equiv \frac{1}{2}\left\langle \mathbf{B}^2(\mathbf{r},t)\right\rangle - \frac{1}{2}\left\langle \mathbf{B}^2(\mathbf{r},0)\right\rangle, \tag{7c}$$

$$G \equiv \langle \rho(\mathbf{r},t)\Phi(\mathbf{r},t)\rangle - \langle \rho(\mathbf{r},0)\Phi(\mathbf{r},0)\rangle\,, \tag{7d}$$

$$U \equiv \frac{1}{\gamma-1}\langle p(\mathbf{r},t)\rangle - \frac{1}{\gamma-1}\langle p(\mathbf{r},0)\rangle = E - K - M \tag{7e}$$

$$OD \equiv \int_0^t \left\langle \eta\mathbf{J}^2(\mathbf{r},t')\right\rangle dt'. \tag{7f}$$

The brackets define the volume averaging, i.e., $\langle q\rangle \equiv 1/V \int_V q \cdot dV$, where q is a physical quantity and V denotes the considered volume. Volume averages are taken over the entire loop structure as well as over the coronal part, with the latter being defined as the volume between the planes $z = 0.2L$ and $0.8L$. In the definition of the gravitational energy the gravitational potential Φ ($\mathbf{g} = -\nabla\Phi$) is used. The potential is set to zero at the chromospheric end-planes.

To check the accuracy of the numerical code, we resort to a standard procedure that relates the inflow of Poynting flux, $\mathbf{S} = \mathbf{E} \times \mathbf{B}$, and kinetic, gravitational, and internal energy to the increase of the total energy, the gravitational energy, and the losses. Using Eq. (1c) and $\mathbf{E} = \eta\mathbf{J} - \mathbf{v} \times \mathbf{B}$, this energy balance equation is easily shown to be

$$-\frac{1}{V}\int_0^t \int_A \mathbf{S}\cdot d\mathbf{A}dt' - \frac{1}{V}\int_0^t \int_A \left(\frac{1}{2}\rho\mathbf{v}^2 + \rho\Phi + \frac{\gamma}{\gamma-1}p\right)\mathbf{v}\cdot d\mathbf{A}\,dt' =$$

$$E(t) + G(t) + \int_0^t \langle \mathcal{L}(t') \rangle \, dt', \tag{8}$$

where A denotes the volume surface. We write Eq. (8) symbolically as

$$S_{\rm tot} + F_{\rm tot} = E + G + L_{\rm tot}. \tag{9}$$

Since this equation contains both volume and surface integral quantities, it provides an excellent test of the accuracy of the numerical method. Figure 2 shows the evolution of the energetic quantities as integrated over the entire loop. The energy balance $S_{\rm tot} = E + G$ for runs 1, 2, 3, 5, and 6 and $S_{\rm tot} = E + G + L_{\rm tot}$ for run 4 is satisfied to within 1%. Figure 3 considers only the coronal part, so that the full energy balance equation applies.

Note, that although the Ohmic dissipation OD does not occur explicitly in the energy balance (it does so implicitly via the total energy E), it is the energetic quantity that is used to measure the efficiency of the conversion of kinetic K and magnetic energy M into internal energy U by means of resonant absorption (see section 3.2).

The evolution of the energetic quantities for runs 1–6 is shown in Figs. 2–3. The most striking features are the strong increase of the internal energy U and the large period oscillations which are most pronounced in the evolution of the coronal averaged quantities (Fig. 3). In section 3.1.1, we argue that these are related to slow magnetosonic oscillations. Also, the buildup of kinetic and magnetic energy that is so typical for the continuous build up of the velocity and magnetic field amplitudes in the resonant layer is only present in the first few driving periods. Section 3.1.2 addresses the resonance layer dynamics. Furthermore, for runs 1–2 and to a lesser extend for run 3, it is apparent that M start to decrease linearly with time after a few driving periods and that it even becomes negative. This will be explained in section 3.1.3.

3.1.1. Slow magnetosonic oscillations

The large time-scale oscillations are related to slow magnetosonic waves that are nonlinearly generated by the Alfvén waves. These waves are compressible and lead to considerable density perturbations as can be seen in Fig. 4, where we have plotted density variations for three different coronal volumes. The density variation, $\delta\rho/\rho$, is defined as

$$\delta\rho/\rho \equiv \frac{\langle \rho(\mathbf{r},t) \rangle - \langle \rho(\mathbf{r},0) \rangle}{\langle \rho(\mathbf{r},0) \rangle}. \tag{10}$$

Oscillations are clearly visible and for runs 3 and 5 (panels (c) and (e) in Fig. 4) the first overtone is even visible. For the three different coronal volumes the oscillations are nicely in phase. This is strong evidence for a standing compressional wave. A Fourier decomposition of the density oscillations of run 3 and 5 show amplitude peaks at periods of 290 s and at 145 s (i.e., the first overtone). The periods agree well with the expression for the fundamental ($n = 1$) and first harmonic ($n = 2$) slow magnetosonic periods $2nL_{\rm cor}/c_{\rm sound}$, where we have substituted the sound velocity $c_{\rm sound}$ as an estimate for the slow magnetosonic wave speed in the low-beta corona. Taking $L_{\rm cor} = L - 2z_{\rm t} = 19.1 \times 10^6$ m for the length of the coronal cavity and substituting the average coronal sound speed at $r = 0.6$ (the radius at which our driver profile reaches its maximum amplitude), $c_{\rm sound} = 126$ km/s, we obtain a period of 301 s.

Besides the oscillations, a growth trend is visible in the density variations (run 1 to 3 or panels (a) to (c)). The trend scales linearly with the driver amplitude whereas the amplitude of the oscillations scale quadratically. The latter is a clear indication of the nonlinear character of the compressional motions. The density variations are larger for runs with longer periods (compare run 3 panel (c) with run 5 in panel (e)). Although not shown here, the variation of the volume averaged coronal temperature exhibits more or less the same growth trend as the density variations. For example, the average temperature has risen with approximately 10% at the end of the simulation of run 3. Due to the low efficiency of resonant absorption, see below in section 3.2, this rise is solely due to compression.

The density variations are larger for the runs with longer driver periods. This is also apparent in the corresponding variations of E, U, and $F_{\rm tot}$ in Figs. 2 and 3. However, for $P_{\rm d} = 66.7$ s the density variations for the coronal volume bounded by $0.2 < z/L < 0.8$ are extremely large with a maximum value over 80%. This huge variation is caused by a significant upward and downward motion of the transition region. To a lesser extend this is also visible in the first 400 s in Fig. 4e for $P_{\rm d} = 53.4$ s. The inclusion of the radiative and conductive losses also leads to large motions of the transition region and consequently to large variations in density, see Fig. 4d. Note, that even for a driver amplitude of 5.9 km/s the density oscillations are still of the order of 0.5%. This should have noticeable observational effects. We will come back to this point in section 4.

3.1.2. Resonant layer and transition region dynamics

Since the build up of kinetic K and magnetic energy M more or less saturates after approximately two to three driving periods, the amplitudes at the resonant position will not have had the time to grow large. Consequently, the gradients will not reach large values either which explains the low Ohmic dissipation rates obtained in all our simulations. For run 3 the evolution of the resonant layer can be followed in the bottom panels of Figs. 5 where different snapshots of the spatial variation of v_θ are plotted. The resonant layers are identified as the positions where the intensity is strongest. The amplitudes can indeed be seen to vary only slightly after the initial two driving periods (the first frame). Furthermore, it is clear that only in the first 3.5 driving periods (the first two frames) one can speak of a single, well defined resonant layer at $r \approx 0.7$. The evolution after 3.5 driving periods becomes very complicated: The upward and downward motions of the transition region and the inflow of mass into the corona will lead to shorter longitudinal wavelengths and shifting of the resonant position. This shift and wavelength shortening are particularly evident if one compares the second frame of v_θ with the last frame.

The upward and downward motions of the transition regions are clearly visible in the upper panel of Fig. 5 which shows the logarithm of the temperature. The motions are non-zero in the radial interval in which the excitation profile is non-zero. In the last time frame both transition regions have been lifted considerably in the interval $0.4 < r < 0.8$. The lift is approximately 2 Mm. This correspond to a change in cavity length of as much as 20%. Since the local Alfvén continuum frequencies are inversely proportional to the cavity length, the shortening of the cavity length will increase them. The Alfvén continuum frequencies increase from the loop axis to the boundary and, hence, the radial position at which the driving frequency matches one of them shifts towards the axis. This shift is visible in the bottom panel of Fig 5 where the maximum value of v_ϕ moves from $r \approx 0.7$ towards $r \approx 0.55$.

For run 1 with four times smaller driving amplitude than run 3 the motions of the transition regions are much smaller ($< 1\%$). Consequently, the tuning and detuning of the cavity is much less of an issue for smaller driver amplitudes. However, the fast saturation of the kinetic and magnetic energy buildup in the resonant layer occur in all our simulations. Two likely causes are (i) wave energy leakage out of the coronal cavity, and (ii) efficient nonlinear generation of slow magnetosonic motions which will result in consumption of most of the incoming Poynting flux in the chromosphere and transition region. It is hard to quantify which of those causes is the most important, but based on the following two arguments we conclude that the efficient nonlinear generation of slow magnetosonic modes must be the most important one.

First, within the linearized ideal MHD framework using a three layer model, it has been shown that wave leakage out of the coronal cavity leads to an asymptotic stationary state with a finite amplitude in the resonant layer (Berghmans & De Bruyne 1995). The time it takes for the amplitude to grow to within a factor ϵ of its asymptotic value is given by $\tau_{\rm as} = \frac{1}{2}P_{\rm d}(\ln\epsilon + \ln(1-R^2))/\ln R$, where R is the reflection coefficient of the Alfvén speed discontinuity. For our model $R \approx 0.8$. The time it takes, then, to grow to within 10% of the asymptotic value is $\tau_{\rm as} = 7.4\,P_{\rm d}$. This is significantly larger than the above mentioned two to three driving periods.

Second, in all simulation runs the initial rise of the internal energy U is strongly related with the kinetic energy K. This is especially clear for the volume averaged coronal quantities in Fig. 3. As soon as the kinetic energy reaches its maximum, after two to three driving periods, the internal energy starts to increase quickly. At the same time, the total inflow of energy into the corona, $F_{\rm tot}$, starts to increase as well. After 2.5 driving periods $F_{\rm tot}$ is already larger than $S_{\rm tot}$. This is indicative of the rapid pace at which energy is transferred from the Alfvén wave to the magnetosonic waves in the chromosphere and transition region. Note also, that the overall rate at which $F_{\rm tot}$ increases is larger than $S_{\rm tot}$ with the exception of run 4, the run with losses taken into account.

In the middle panel of Fig. 5 the nonlinear evolution of the longitudinal velocity component v_z is plotted. The initial evolution shows v_z having a longitudinal wavelength approximately twice as large as v_θ. This wavelength doubling agrees well with results from weakly nonlinear theory applied to a uniform line-tied plasma (e.g., Nakariakov 1997). Due to the large chromospheric driver amplitude the nonlinearly generated v_z perturbations will quickly develop into shocks as can easily be seen from the third frame on. The shocks are slow magnetosonic (the magnetic field is rotated towards the shock front normal, not shown here). As a consequence of our chosen longitudinal boundary conditions, those shocks that have not been reflected at the transition region will be reflected at the chromospheric boundaries. Hence, the spatial evolution becomes very complicated consisting of multiple upward and downward propagating shocks. These interacting internal shocks occur only for sufficiently non-linear driver amplitudes, as no shocks were observed in run 1.

3.1.3. Magnetic flux decay

In this subsection we briefly discuss the numerical cause for the decrease in magnetic energy with time that is clearly visible in the plots for runs 1 and 2 (Figs. 2a, 2b and Figs. 3a and 3b; the decrease also appears in the other runs but is less visible). The decrease in magnetic energy even makes M negative in those runs which means that the magnetic energy is less than in the initial state. This behavior is neither due to diffusion nor to a nonlinear conversion of the free magnetic energy. Instead, a close inspection shows that at the same time the kinetic energy saturates the energy stored in the azimuthal magnetic component is saturating as well and that only the energy in the longitudinal component is decreasing. We found that this decrease in the longitudinal component is due to a decrease of the magnetic flux, $\phi = 2\pi \int_0^1 B_z r dr$, through the chromospheric end-planes. The evolution of ϕ is governed by

$$\frac{d\phi}{dt} = 2\pi \left(v_z B_r - v_r B_z - \eta J_\theta\right)_{r=1}. \tag{11}$$

As a consequence of our chosen boundary conditions, all terms on the right-hand side should be identically zero and, hence, the flux should remain constant at all times. In reality, however, the second term, being a derived quantity (the curl of B has to be calculated), will result in a small but non-zero value of $d\phi/dt$. In our case it is negative and it leads to a gradual, though slow, decay of the longitudinal magnetic field, viz., $\delta B_z/B_z \approx 10^{-5}t$. Note, that the loss of magnetic flux does not violate the requirement that the divergence of the magnetic field has to be zero; the flux loss is constant throughout the loop structure.

3.2. Efficiency of resonant absorption

We have shown that the evolution of the energetic quantities reveals that most of the Poynting flux that is injected into the loop structure is used to support mass motions from the chromosphere into the corona, effectively compressing the coronal plasma. This already indicates that the heating by resonant absorption is low.

There are many ways to express the efficiency of resonant absorption. Here, we largely follow Poedts & Boynton (1996) in the use of absorption, dissipation, and quality coefficients. These authors divide the Poynting flux into terms representing in- and outflow, viz., $S(t) = S^{+}(t) - S^{-}(t)$, where

$$S(t) = -\frac{1}{V}\int_A \mathbf{S}\cdot d\mathbf{A} \tag{12a}$$

$$S^{+}(t) = \begin{cases} S(t), & S(t) \geq 0. \\ 0, & S(t) < 0. \end{cases} \tag{12b}$$

$$S^{-}(t) = \begin{cases} 0, & S(t) \geq 0. \\ -S(t), & S(t) < 0. \end{cases} \tag{12c}$$

The corresponding time integrated quantities are denoted by the subscript total and are given by:

$$S_{\rm tot}(t) = \int_0^t S(t')\,dt', \tag{13a}$$

$$S^{+}_{\rm tot}(t) = \int_0^t S^{+}(t')\,dt', \tag{13b}$$

$$S^{-}_{\rm tot}(t) = \int_0^t S^{-}(t')\,dt'. \tag{13c}$$

Due to the chosen boundary conditions, the Poynting flux is zero at the radial boundary. Inspection shows that the Poynting flux always points outwards at the $z = L$ chromospheric boundary. Hence, S^{+} is determined by Poynting flux through the $z = 0$ chromospheric plane only. Therefore, S^{+} can be linked with the energy supplied by the driver.

3.2.1. The absorption coefficient

Poedts & Boynton (1996) have defined an absorption coefficient

$$\alpha_a \equiv \frac{S_{\rm tot}}{S^{+}_{\rm tot}} \tag{14}$$

that measures the amount of energy that is absorbed with respect to the energy supplied by the driver. For the simulation of resonant absorption in line-tied loops higher values of the absorption coefficient indicate better coupling of the incoming wave with the coronal plasma and better heating efficiency since higher fractions of the incoming flux are absorbed. However, whereas values near one can be obtained within line-tied models, much smaller values will be obtained when coronal loops are properly modeled as interference filters: $\alpha_a \propto c_{\rm a,chromosphere}/c_{\rm a,corona}$ near transition maxima (see Eq. (48) in Hollweg 1984b). When the corona is a perfect cavity, i.e., when the ratio of the chromospheric to coronal Alfvén speeds, $c_{\rm a,chromosphere}/c_{\rm a,corona}$, is zero, α_a is zero. As shown by Hollweg (1984b) using a three layer loop model, this behavior is due to a destructive interference between the reflected (downwards going) incident waves and the waves leaking out of the cavity.

For our different simulation runs, α_a is plotted in Fig. 6a. For all runs, α_a starts at 1.0 and then drops quickly between the second and fifth driving period to reach a more or less stationary state. In this time interval waves that are twice transmitted at the transition region have reached the 'other' chromospheric boundary and leave the loop system leading to an outflow of Poynting flux. Also, after approximately 3.5 driving periods the above mentioned destructive interference will become important.

From the graphs of runs 1–3, it is clear that the absorption coefficient reaches a constant value, $\alpha_a \approx 0.3$, and that it has a very weak dependence on the driver amplitude. This weak dependence on driver amplitude is to be expected since the properties of the interference filter do not depend on it (at least in the linear regime).

The absorption coefficients for runs 5 and 6 exhibit an oscillatory behavior which is due to the relatively large upward and downward motions of the transition region. These simulation runs do, however, appear to reach a stationary value as well, viz., $\alpha_a \approx 0.3$ for $P_{\rm d} = 53.4$ s and $\alpha_a \approx 0.5$ for $P_{\rm d} = 66.7$ s. This also holds true for the run with inclusion of the losses for which α_a oscillates around the stationary value of the same run without the losses. Hence, all the simulation runs with driving frequencies within the Alfvén continuum (which, therefore, lead to resonant absorption) have more or less the same stationary value. However, run 6, with a frequency not located in the continuum range has a significantly higher stationary value. Why the absorption coefficient is higher in this case is not completely clear to us. The fact that the driving frequency does not match an eigenfrequency of the corona and the fact that the frequency is lower so that it is easier for the heavy chromospheric and transition region plasma to follow the driven oscillations must play an important role (the lifting of the transition region is indeed much larger for run 6 when compared to run 3 and 5).

3.2.2. The dissipation coefficient

The dissipation coefficient measures the amount of Ohmic dissipation relative to the total absorbed Poynting flux:

$$\alpha_d \equiv \frac{OD}{S_{\rm tot}}. \tag{15}$$

The higher this coefficient is the more efficient the heating process. We deviate here from the definition by Poedts & Boynton (1996) by using the Ohmic dissipation in the numerator instead of the change in internal energy. In their model runs, the increase in internal energy is almost entirely due to Ohmic dissipation in the resonant layers and, hence, the same information is obtained by either using the internal energy or the Ohmic dissipation. Since this is not the case for our simulations, we have exploited the Ohmic dissipation, being the more natural choice, in the definition of the dissipation coefficient.

We have plotted α_d considering the Ohmic dissipation in the whole loop structure in Figs. 6b and considering only the coronal part in Fig. 6c. From these figures we observe the following.

First, only between 5 and 10 percent of the total Poynting flux is converted into Ohmic dissipation in the corona. Combined with the information of the absorption coefficient this means that only a few percent of the power supplied by the driver is converted into heat. Clearly, heating of the corona by resonant absorption is very inefficient.

Second, the Ohmic dissipation in the chromosphere and the transition region is approximately a factor 4 to 8 higher than in the corona. Hence, heating of those regions is much more efficient than heating of the coronal part of the loop.

Third, α_d is smaller for larger driver amplitudes. This is in agreement with the picture sketched in the previous subsection: the amplitudes of the nonlinearly generated slow magnetosonic modes scale quadratically with the driver amplitude. Consequently, higher fractions of the Poynting flux are used to generate these modes and to support the related compressional motions.

Fourth, comparing the run with inclusion of the losses with the same one without shows that the dissipation coefficient can be significantly higher. At the end of the simulation, $t \approx 600$ s it is between 1.5 and 2 times larger.

Fifth, except for the run that includes the losses, the dissipation coefficients appear to reach stationary values just as in the case of the absorption coefficient. For the run that includes the losses the dissipation coefficient appears to grow linearly in time. However, it is still possible that stationary values are reached when the simulation is extended.

Sixth, the runs with larger driver period produce more Ohmic dissipation in the chromosphere and transition region.

3.2.3. The quality factor

The last figure we use to quantify the efficiency is the quality factor. It is defined as the ratio of stored energy over the Ohmic dissipation in one driving period, viz.,

$$Q \equiv \frac{E+G}{\int_t^{t+P_\mathrm{d}} \langle \eta \mathbf{J}^2(t') \rangle \, dt'}. \tag{16}$$

Within the linearized MHD framework, the quality has been used extensively by Poedts et al. (1994) in the study of stationary, side ways driven one-dimensional coronal loop models. For those models the quality factor is related to the quality of the resonance. Since completely stationary states are not obtained in our simulations the connection is hard to make. The quality factor basically tells us within how many driving periods Ohmic dissipation will consume all the stored energy once the driving is stopped. The lower the number of periods the better the efficiency of the heating.

Quality factors for the total loop volume and the coronal volume are shown in Figs. 6d and

6e. The most noticeable feature is that while the quality factor for the runs without inclusion of the loss functions exhibits a growing trend (this trend only shows up for $t > 200$ s) the quality factor for the run with the inclusion of the loss function clearly has a decreasing trend leading to low values, $Q \approx 10$.

The growing trend in the runs without the inclusion of the losses is due to the fact that the Ohmic dissipation rate reaches a constant value while the stored energy keeps on growing. The initial decrease of Q in Fig. 6d, is caused by an increase of the (volume averaged) Ohmic dissipation rate that is faster than the increase of the stored energy. The minima of the quality factors for the different runs in Fig. 6e correspond to the maximum Ohmic dissipation rates. The quality factor for the run with inclusion of the losses exhibit a decreasing trend because the dissipation rate grows with time and the stored energy reaches a maximum at $t \approx 7.5\,P_{\rm d}$ after which it decreases again.

4. Relevance for coronal brightenings

The fact that the slow magnetosonic waves are so effectively generated is of relevance for the interpretation of some coronal and transition region observations.

Recently, Ireland et al. (1999) have observed active region oscillations with the Coronal Diagnostic Spectrometer (CDS) aboard the Solar and Heliospheric Observatory (SOHO). The observations were performed using emission lines that are formed in the chromosphere, the transition region, and the corona. In the transition region lines they find significant power for periods of 300 s, whereas in the corona power is located around 100 s, 200 s, and 400 s. If it is assumed that the oscillations originate in active region loops then they may very well be explained by an Alfvén wave train just as in our model. Especially, the observed frequency doubling in the corona fits in well and, based on the density variations of our simulation runs 1–3, suggest a relatively large Alfvén wave amplitude in the chromosphere to excite the double frequencies.

The recent observations of coronal and transition region brightenings using the Extreme ultraviolet Imaging Telescope (EIT) aboard SOHO (Berghmans, Clette, & Moses 1998) can also be explained by mass motions which are nonlinearly generated by Alfvén waves. Both the linear relation between the area of the brightening and its duration, and the amount of energy radiated away during the brightening, can be accounted for in our model. Taking the on-side surface of loops $\propto aL$ as the area of the brightenings the linear relationship follows if we substitute the slow wave period, $P = 2L_{\rm cor}/c_{\rm sound}$, for the duration of the brightenings. The additional energy radiated away in a brightening is of the order of the quiet radiative energy loss. In Fig. 7, the variation of radiative losses for run 4 is plotted for three different coronal volumes. The variations in the losses for the smallest $(0.4 < z/L < 0.6)$ and the largest volume $(0.2 < z/L < 0.8)$ are approximately 2.5 times larger than in the initial state. The variation of the radiative losses is so much higher for the volume $0.3 < z/L < 0.7$ because of the upward motion of the transition region and mass deposition in the region $0.3 < z/L < 0.4$. Based on the variations in radiative energy losses for $0.2 < z/L < 0.8$, we estimate that for driver amplitudes of approximately 10 km/s the observed variation in the radiative losses will be obtained in our model.

5. Discussion and Conclusions

In this we paper we investigated numerically the nonlinear MHD evolution of coronal loops that are excited by linearly polarized monochromatic Alfvén waves at the chromospheric level. What sets our model aside from previous models is that variations across and along the magnetic field are taken into account. The variation along the magnetic field is dominated by the thermal structuring of the transition region and chromosphere. Hence, the transition region is free to move and mass motions from the chromosphere to the corona can take place. Loops are modeled as finite length axisymmetric cylinders with the ends representing the chromosphere and the mid-plane the coronal loop tops. Simulations with different excitation amplitudes and excitation frequencies have been carried out as well as one simulation for which optically thin radiative losses and thermal conduction have been taken into account.

When the loops are excited at the chromospheric level with a frequency that is located in the ideal MHD continuum the resulting resonant absorption is far less efficient than has been concluded previously for studies of resonant absorption in line-tied loop systems. The efficiency has been expressed in terms of the absorption and dissipation coefficients, α_a and α_d, respectively, and the quality factor Q. The absorption coefficient converges to a value of 30%. Hence, only 30% of the incoming Poynting flux is absorbed within the loop structure. Of this 30% only 5% to 10% is converted into heat in the corona with larger excitation amplitudes converting less. The coronal quality factor increases in time with values between 150 and 200 at the end of our simulations ($t \approx 900$ s). This growth of the quality is due to the Ohmic dissipation rate reaching a constant value after only a few driving periods while the stored energy keeps on growing.

Remarkably, when optically thin radiative losses and thermal conduction are taken into account, the efficiency improves. Instead of increasing in time, the quality factor decreases and values of $Q \approx 20$ are obtained at the end of the simulation. Also the dissipation coefficient grows linearly in time and does not appear to approach an asymptotic value as is the case for the simulations without the losses. After 600 s it is already a factor two larger in the corona. Since the Ohmic dissipation acts as an additional heating source (recall that a heat source of unspecified nature had to be assumed to balance the losses in the initial state), the effects of the loss function $\mathcal{L}$ on the loop dynamics are such that it enhances the Ohmic heating. The above shows the extreme impact of the loss function on the Ohmic heating efficiency.

Coronal cavity leakage, cavity detuning by the upward and downward motions of the transition region, and the nonlinear energy transfer from the Alfvén waves to the magnetosonic waves cause the efficiency of the resonant absorption process to be much lower than in equivalent line-tied models (see, for example, Poedts & Boynton (1996)). Based on the evolution of the energetic quantities we have shown that the energy transfer to the magnetosonic waves is the dominant cause. The transfer is very efficient in the chromosphere and transition region.

In our simulations we have found that slow magnetosonic waves are predominantly generated by Alfvén waves. The frequency of these waves corresponds well with the fundamental slow wave mode that fits in the coronal cavity and, not surprisingly, it does not depend on the frequency with which the loop is excited at the chromospheric level. The compressive nature of the slow waves gives rise to density oscillations. Their amplitudes scale quadratically with the amplitude of the driver, which is a restatement of their nonlinear origin. For a moderately small driver amplitude of 5.9 km/s the volumetric averaged coronal density oscillations amount to 0.5%. This is large enough to lead to detectable changes in observed coronal and transition region emission intensities. In the context of solar wind acceleration by solitary waves that are nonlinearly generated by Alfvén waves Offman & Davila (1997) have found similar results. In addition to the Alfvén fluctuations they also found large density fluctuations that are due to the solitary waves.

Besides the density oscillations our results show that mass is being transported into the corona. The deposition of mass is largest in the early stages of the simulations. At the end it has been significantly reduced. The deposition of mass appears as a trend in the density variations. Its scaling with the driver amplitude is linear. Like the density oscillations the deposition of mass in the corona will lead to changes in observed emission intensities.

Our results support the idea for indirect coronal heating by the nonlinear generation and dissipation of compressional magnetosonic waves (Wentzel 1978; Hollweg 1981; Hollweg et al. 1982). As shown by Wang (1997), the dissipation of slow magnetosonic plane waves is extremely strong in the corona due to very small values of β and the large thermal conduction coefficient. For typical coronal β values it will be two to three orders of magnitude higher than the equivalent dissipation rates of Alfvén and fast magnetosonic waves. Furthermore, although the efficiency of resonant absorption is low, the average coronal temperature still rises significantly due to the induced compression.

Finally, we have pointed out that the slow magnetosonic waves and the associated density oscillations can be used to explain some recently observed transition region and coronal intensity brightenings when these brightenings are assumed to occur in closed loop structures.

Although our results indicate that the chromospheric coupling effects lead to resonant absorption with efficiencies much lower than reported in previous studies for line-tied loop models, it is premature to rule out resonant absorption as a possible heating mechanism for the solar corona. More model simulations are needed that take into account: (a) larger chromospheric regions, (b) larger loop lengths, (c) the divergence of the magnetic field in the chromosphere, (d) the dependence on the azimuthal coordinate, (e) a more realistic broad band excitation spectrum, (f) different density and temperature scalings of the heat source in the loss function $\mathcal{L}$. Inclusion of these effects will allow us to better quantify leakage effects (item a), the coupling to global modes (item d), and Kelvin-Helmholtz and resistive instabilities (also item d).

The authors wish to thank M. van Aalst and J. Ireland for many fruitful discussion on the subjects of this paper.

The development of the Versatile Advection Code has been carried out as part of Massive Parallel Computing, Computational Magneto-Fluid Dynamics programme (cluster project 95MPR04), a programme financed by the 'Nederlandse Organisatie voor Wetenschappelijk Onderzoek' (NWO). A.J.C. Beliën carried out this work as an External ESA Fellow.

The use of supercomputing facilities was sponsored by 'Stichting Nationale Computerfaciliteiten' (National Computer Facilities Foundation (NCF)) and the NASA Center for Computer Services (NCCS) with financial support from NWO and the SOHO project.

REFERENCES

Beliën, A.J.C., Poedts, S., & Goedbloed, J.P. 1997a, A&A, 322, 995

Beliën, A.J.C., Poedts, S., & Goedbloed, J.P. 1997b, Comp. Phys. Comm., 106, 21

Berghmans, D., & De Bruyne, P. 1995, ApJ, 453, 495

Berghmans, D., & Tirry, W.J. 1997, A&A, 325, 318

Berghmans, D., Clette, F., & Moses, D. 1998, A&A, 336, 1039

Braginskii, S.I. 1965, Rev. Plasma Phys., 1, 205

Browning, P.K. 1991, Plasma Phys. Contr. Nucl. Fusion, 33, 539

Davila, J.M. 1987, ApJ, 317, 514

Goedbloed, J.P. 1995, in International Conf. on Plasma Physics, Foz do Iguacu, Brasil, Oct. 31 - Nov. 4, 1994, AIP Conference Proceedings (Am. Inst. Physics) 345, 465

Goossens, M., Ruderman, M.S., & Hollweg, J.V. 1995, Sol. Phys., 157, 75

Grossmann, W., & Tataronis, J.A. 1973, Z. Physik, 261,217

Grossmann, W., & Smith, R.A. 1988, ApJ, 332, 476

Halberstadt, G., & Goedbloed, J.P. 1995a, A&A, 301, 559

Halberstadt, G., & Goedbloed, J.P. 1995b, A&A, 301, 577

Hollweg, J.V. 1981, Sol. Phys., 70, 25

Hollweg, J.V., Jackson, S., & Galloway, D. 1982, Sol. Phys., 75, 35

Hollweg, J.V. 1984a, ApJ, 277, 392

Hollweg, J.V. 1984b, Sol. Phys., 91, 269

Hollweg, J.V., & Yang, G. 1988, J. Geophys. Res., 93, 5423

Hollweg, J.V. 1992, ApJ, 389, 731

Ionson, J.A. 1978, ApJ, 226, 650

Ionson, J.A. 1982, ApJ, 254, 318

Ireland, J., Walsh, W., Harrison, R.A., & Priest, E.R. (1999) accepted for publication in A&A

Kappraff, J.M., & Tataronis, J. 1978, J. Plasma Phys., 18, 209

Kudoh, T. & Shibata, K. 1999, ApJ, 514, 493

Low, B.C. 1975, ApJ, 197, 251

Mariska, J.T., & Hollweg, J.V. 1985, ApJ296, 746

Martens, P.C.H., & Kuin, N.P.M. 1983, A&A, 123, 216

Martens, P.C.H. 1986, in Coronal and Prominence Plasmas, NASA CP-2442, ed. A.I. Poland, 407

Nakariakov, V.M., Roberts, B., & Murawski, K. 1997, Sol. Phys., 175, 93

Ofman, L., Davila, J.M., & Steinolfson, R.S. 1994a, ApJ, 421, 360

Ofman, L., Davila, J.M., & Steinolfson, R.S. 1994b, Geophys. Res. Lett., 21, 2259

Ofman, L., Davila, J.M., & Steinolfson, R.S. 1995, ApJ, 444, 471.

Ofman, L., & Davila, J.M. 1995, J. Geophys. Res., 100, 23427

Ofman, L., & Davila, J.M. 1997, ApJ, 476, 357

Ofman, L., Klimchuk, J.A., & Davila, J.M. 1998, 493, 474

Odstrčil, D. 1990, J. Comp. Phys., 91, 71

Orrall, F.Q., ed. 1981, Solar Active Regions (Boulder: Colorado Associated University Press).

Parker, E.N. 1992, J. Geophys. Res., 97, 4311

Poedts, S., Goossens, M., & Kerner, W. 1989, Sol. Phys., 123, 83

Poedts, S., & Kerner, W. 1992, J. Plasma Phys., 47, 139

Poedts, S., Beliën, A.J.C., & Goedbloed, J.P. 1994, Sol. Phys., 151, 271

Poedts, S., & Boynton, G.C. 1996, A&A, 306, 610

Poedts, S., & Goedbloed, J.P. 1997, A&A, 321, 935

Poedts, S., Tóth, G., Beliën, A.J.C., & Goedbloed, J.P. 1997, Sol. Phys., 172, 45

Powell, K.G., ICASE Report No. 94-24, Langley, VA

Raymond, J.C., & Smith, B.W. 1977, ApJS, 35, 419

Roe, P.L. 1981, J. Comp. Phys., 43, 357

Rossner, R., Tucker, W.H., & Vaiana, G.S. 1978, ApJ, 220, 643

Ruderman, M.S., & Goossens, M. 1993, Sol. Phys., 143, 69

Steinolfson, R.S., & Davila, J.M. 1993, ApJ, 415, 354

Sterling, A.C., & Hollweg, J.V. 1988, ApJ, 327, 950

Sterling, A.C., & Hollweg, J.V. 1989, ApJ, 343, 985

Sterling, A.C., & Mariska, J.T. 1990, ApJ, 349, 647

Tataronis, J.A., & Grossmann, W. 1973, Z. Physik, 261, 203

Tataronis, J.A. 1975, J. Plasma Phys., 13, 87

Tirry, W.J., Berghmans, D., & Goossens, M. 1997, A&A, 322, 329

Tirry, W.J., & Berghmans, D. 1997, A&A, 325, 329

Tirry, W.J., & Poedts, S. 1998, A&A, 329, 754

Tóth, G. 1996, Astrophysical Letters & Communications, 34, 245

Tóth, G., & Odstrčil, D. 1996, J. Comp. Phys., 128, 82

Whang, Y.C. 1997, ApJ, 485, 389

Wentzel, D.G. 1978, Sol. Phys., 58, 307

Wright, A.N., & Rickard, G.J. 1995, ApJ, 444, 458

Zhugzhda, Y.D., & Locans, V. 1982, Sol. Phys., 76, 77

Zirker, J.B. 1993, Sol. Phys., 148, 43

Fig. 1.— Temperature, pressure, and density profiles for our reference initial state: (a) Radial variation at the loop top. (b) Longitudinal variation along the axis. Actual parameter values: (Eqs. (4b)–(4c)) $\theta_1 = -1$, $\theta_2 = 0.5$, $\xi = 0.04$, $z_\mathrm{t} = 0.15L$, and $w_\mathrm{t} = 1.2a$, (Eq. (5b)) $b_1 = -1.5$, $b_2 = 0.75$, and $\beta_\mathrm{chr} = 0.194$.

Fig. 2.— Evolution of the energetic quantities, see section 3.1 for their definition, for the simulation runs of Table 1. (a) Run 1 . . . (f) Run 6. Volume averaging has been performed over the entire loop structure.

Fig. 3.— Same as Fig. 2 but now the volume average has been taken over the coronal volume, $0.2 < z/L < 0.8$, only.

Fig. 4.— Volume averaged density variations for three different coronal volumes, viz., $0.2 < z/L < 0.8$ (solid line), $0.3 < z/L < 0.7$ (dashed line), and $0.4 < z/L < 0.6$ (dot-dashed line).

Fig. 5.— Run 3: spatial and temporal evolution of $\log T$ (top panel), v_z (middle panel), and v_θ (bottom panel). Linear gray scales are exploited. Black and white represent minimum and maximum values, respectively ($4.31 \leq \log T \leq 6.005$, -30.3km/s $\leq v_z \leq 24.2$ km/s, -60.5 km/s $\leq v_\theta \leq 90.8$ km/s). The different frames in each panel correspond to different times with time increasing from left to right: $t = 80.2$ s, $t = 145.0$ s, $t = 278.3$ s, $t = 411.8$ s, $t = 545.1$ s, $t = 678.3$ s, $t = 810.5$ s. In each frame, r is plotted horizontally whereas z is plotted vertically. Note, that only the interval $0.1 \leq r \leq 1.0$ is shown and that the major tick marks are at .2, .4, .6, and .8. In the vertical direction, z runs from 0 at the bottom to L at the top.

Fig. 6.— (a) Absorption coefficient. (b) Dissipation coefficient (c) Same as frame (b) but now for the Ohmic dissipation in the corona only. (d) Quality factor for the whole loop structure. (e) Quality factor for the coronal part of the loop.

Fig. 7.— Variation of the volume averaged optically thin radiative losses for run 4. The same three volume averages are plotted as in Fig. 4.

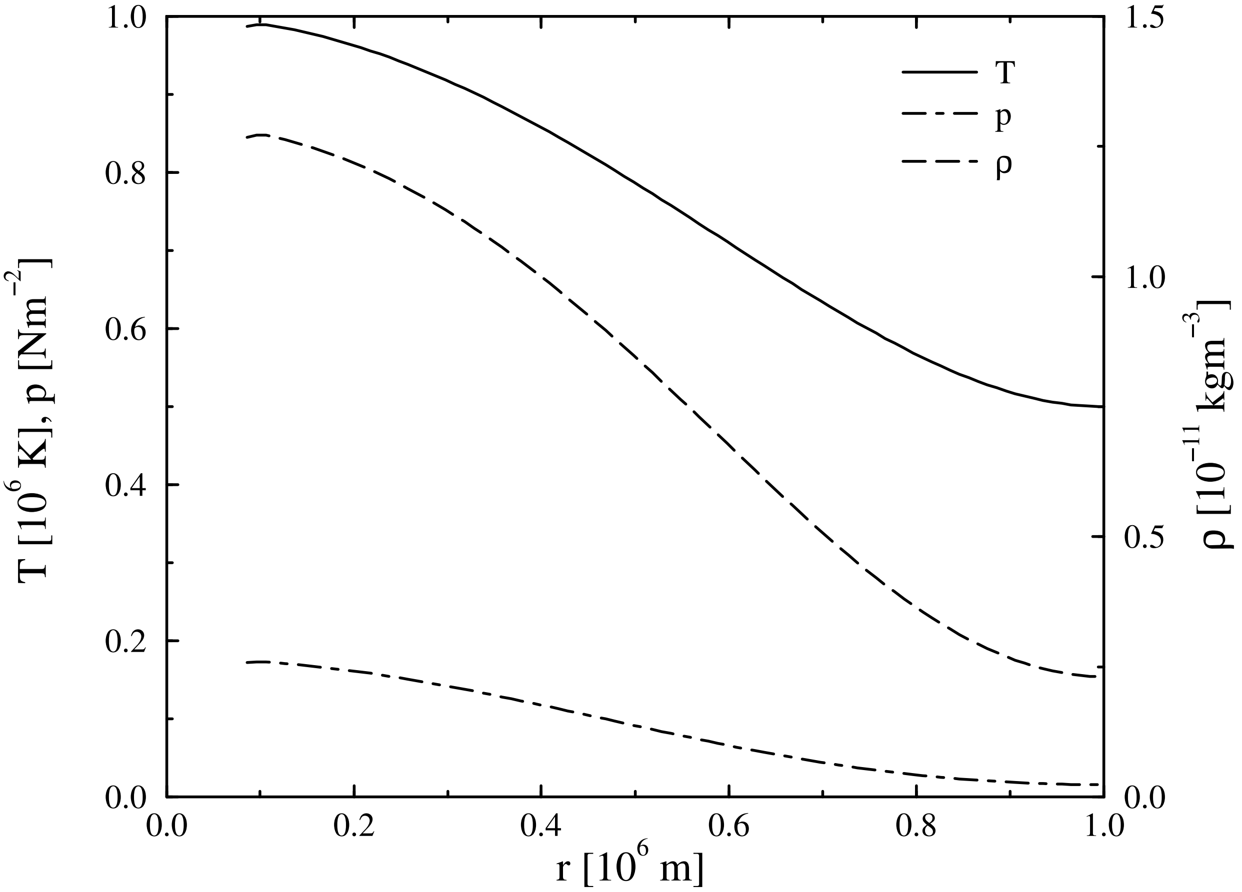

1.0
0.8
0.6
0.4
0.2
0.0
0.0
0.2
0.4
0.6
0.8
1.0
1.5
1.0
0.5
0.0
T
p
ρ
T [10^6 K], p [Nm^−2]
ρ [10^−11 kgm^−3]
r [10^6 m]

Figure 1a

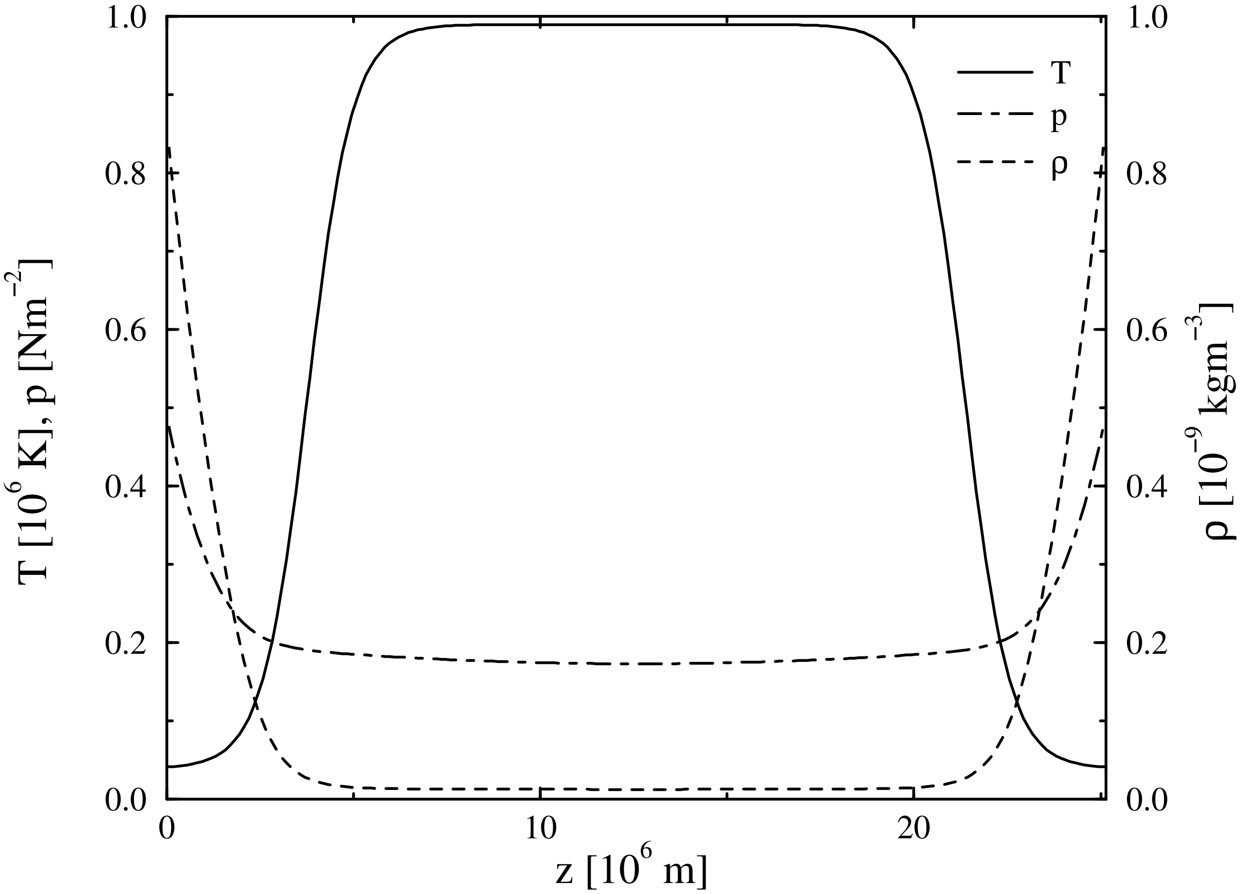

Figure 1b

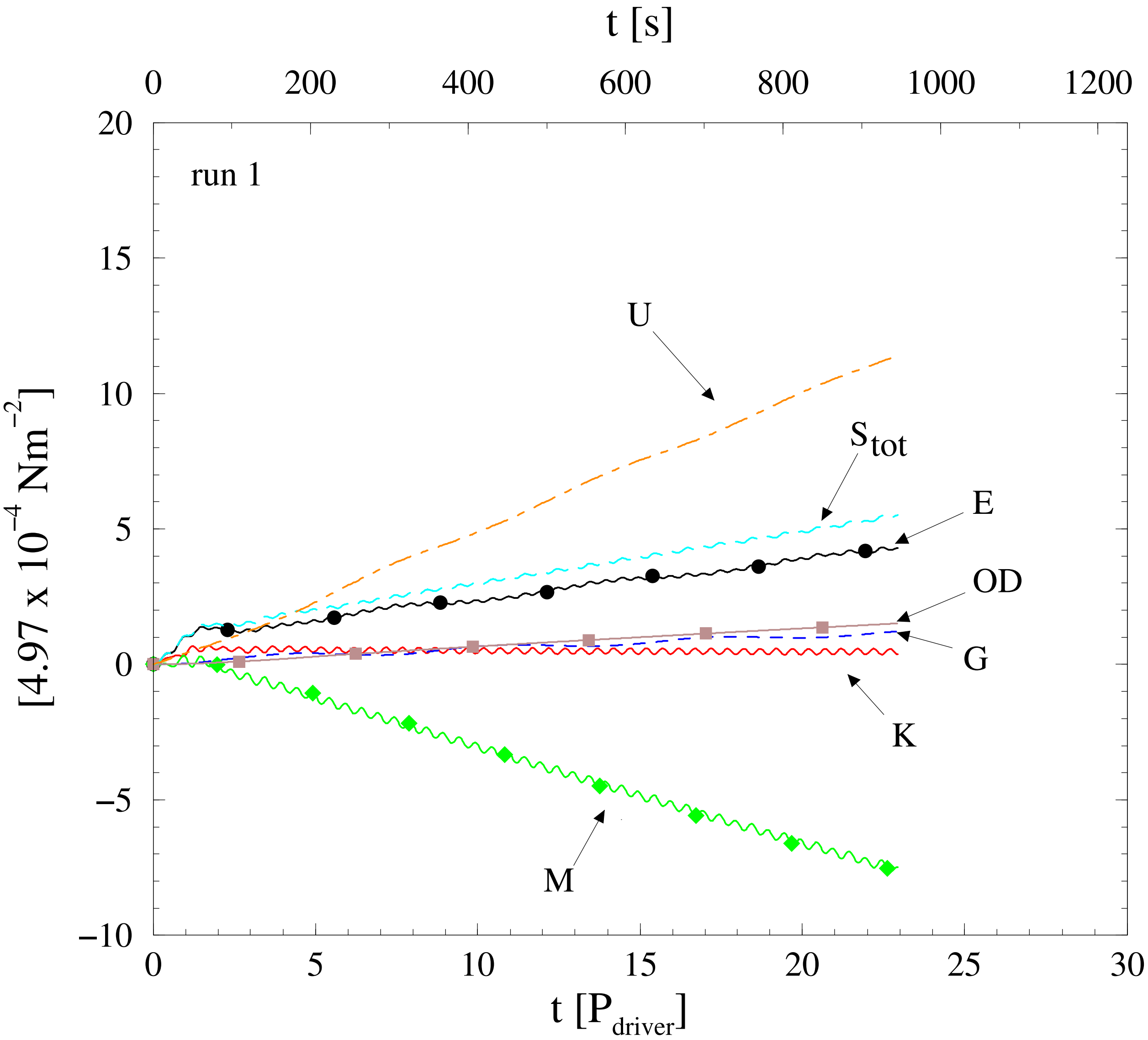
t [s]
0
200
400
600
800
1000
1200
run 1
U
S_{tot}
E
OD
G
K
M
20
15
10
5
0
−5
−10
[4.97 x 10^{-4} Nm^{-2}]
0
5
10
15
20
25
30
t [P_{driver}]

Figure 2a

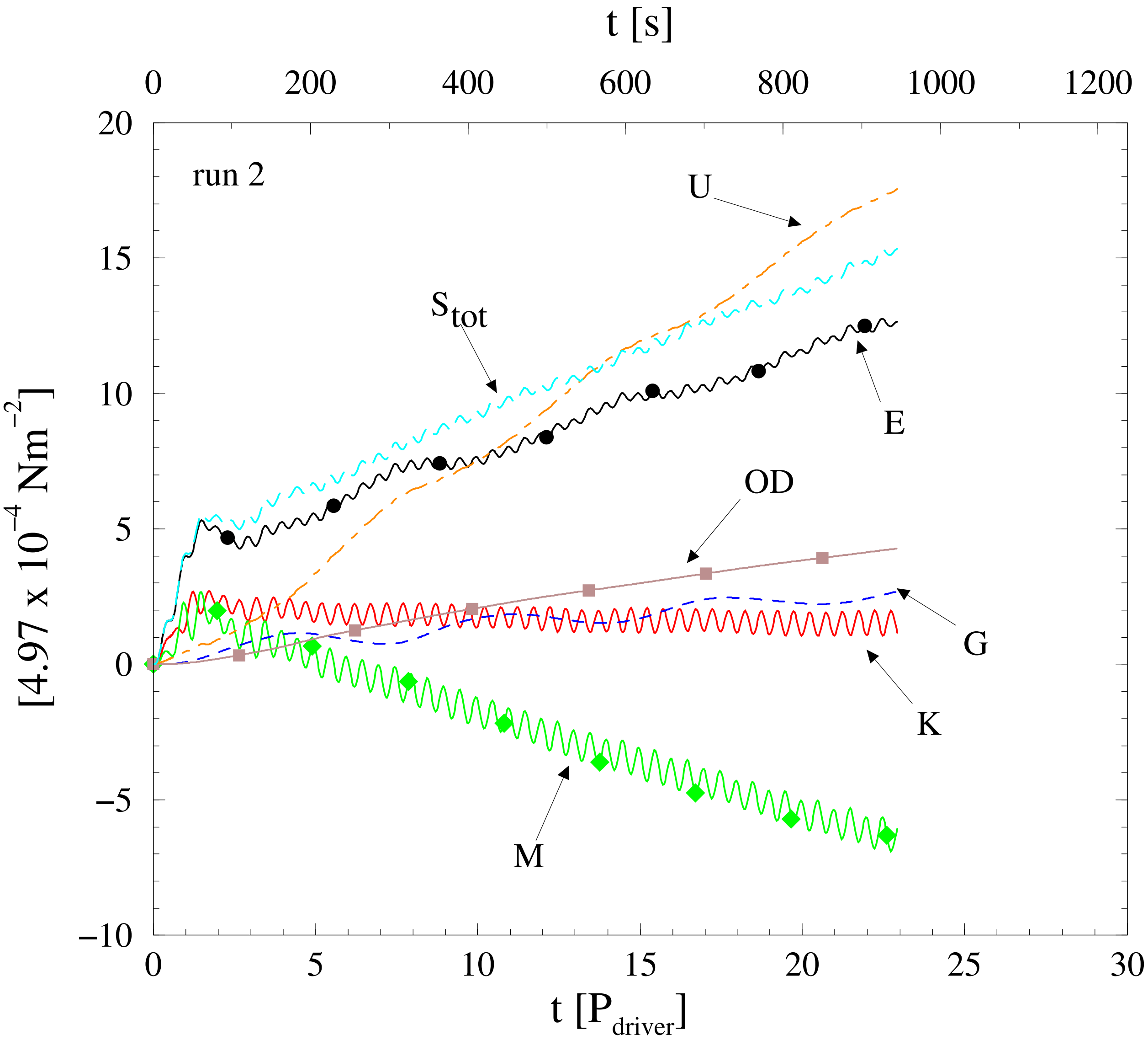
t [s]
0
200
400
600
800
1000
1200
20
15
10
5
0
−5
−10
run 2
U
S_{tot}
E
OD
G
K
M
[4.97 x 10^{-4} Nm^{-2}]
0
5
10
15
20
25
30
t [P_{driver}]

Figure 2b

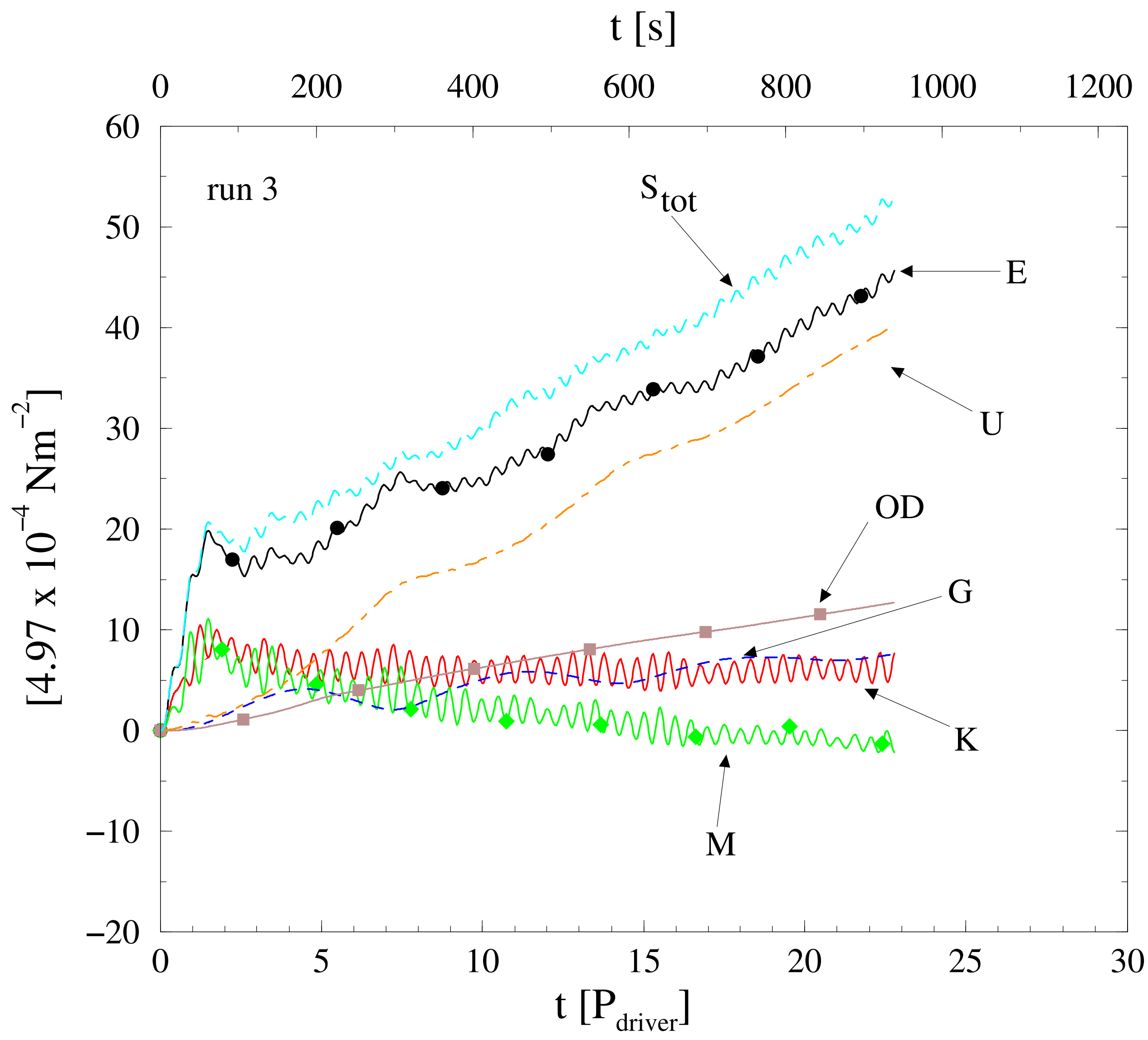
t [s]
0
200
400
600
800
1000
1200
60
50
40
30
20
10
0
−10
−20
run 3
S_{tot}
E
U
OD
G
K
M
$[4.97 \times 10^{-4}\ Nm^{-2}]$
0
5
10
15
20
25
30
t [P_{driver}]

Figure 2c

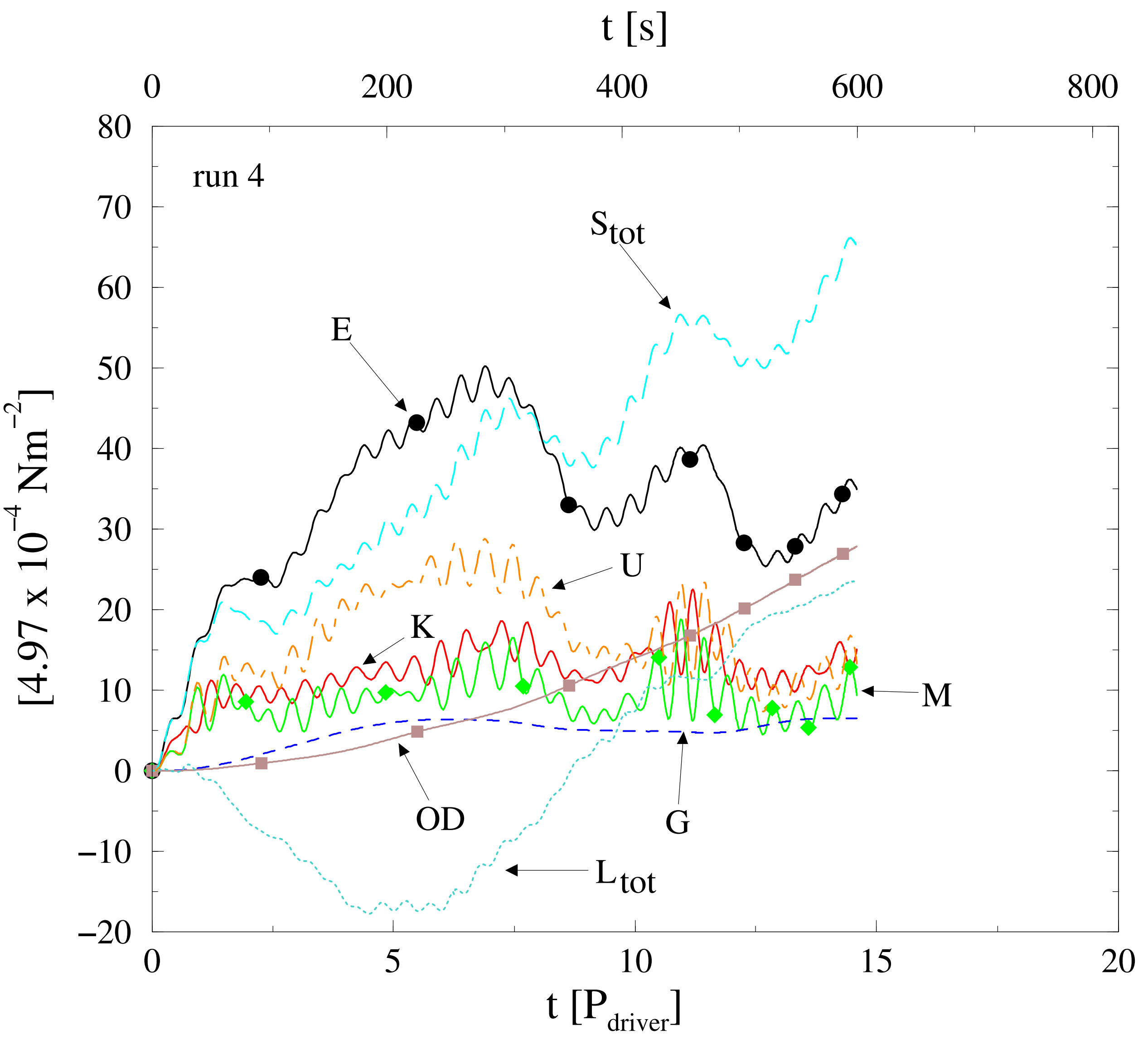
t [s]
0
200
400
600
800
80
70
60
50
40
30
20
10
0
−10
−20
run 4
S_tot
E
U
K
M
OD
G
L_tot
[4.97 x 10^-4 Nm^-2]
0
5
10
15
20
t [P_driver]

Figure 2d

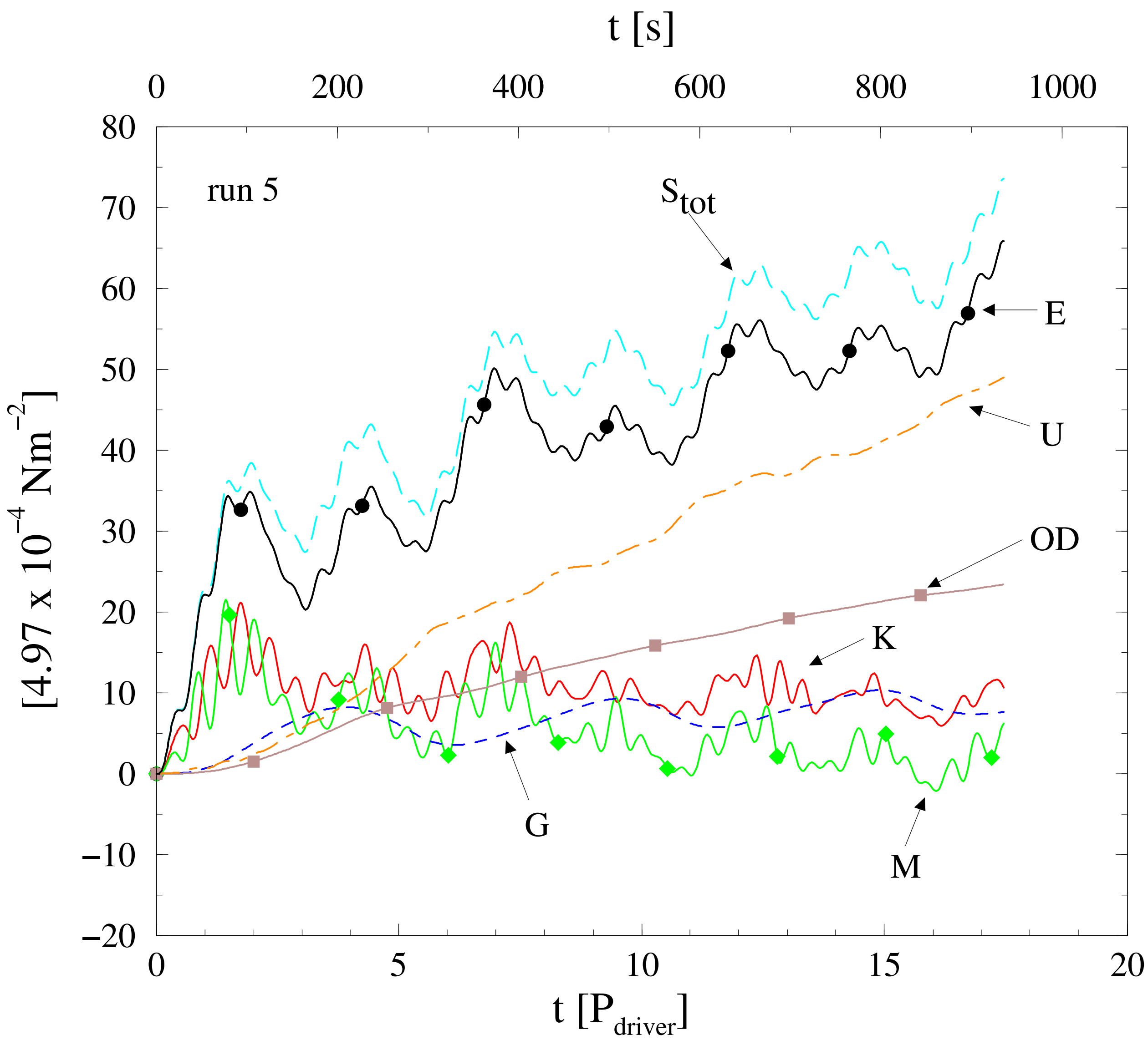
t [s]
0
200
400
600
800
1000
80
70
60
50
40
30
20
10
0
−10
−20
run 5
S_{tot}
E
U
OD
K
G
M
$[4.97 \times 10^{-4}\ \mathrm{Nm}^{-2}]$
0
5
10
15
20
$t\ [P_{driver}]$

Figure 2e

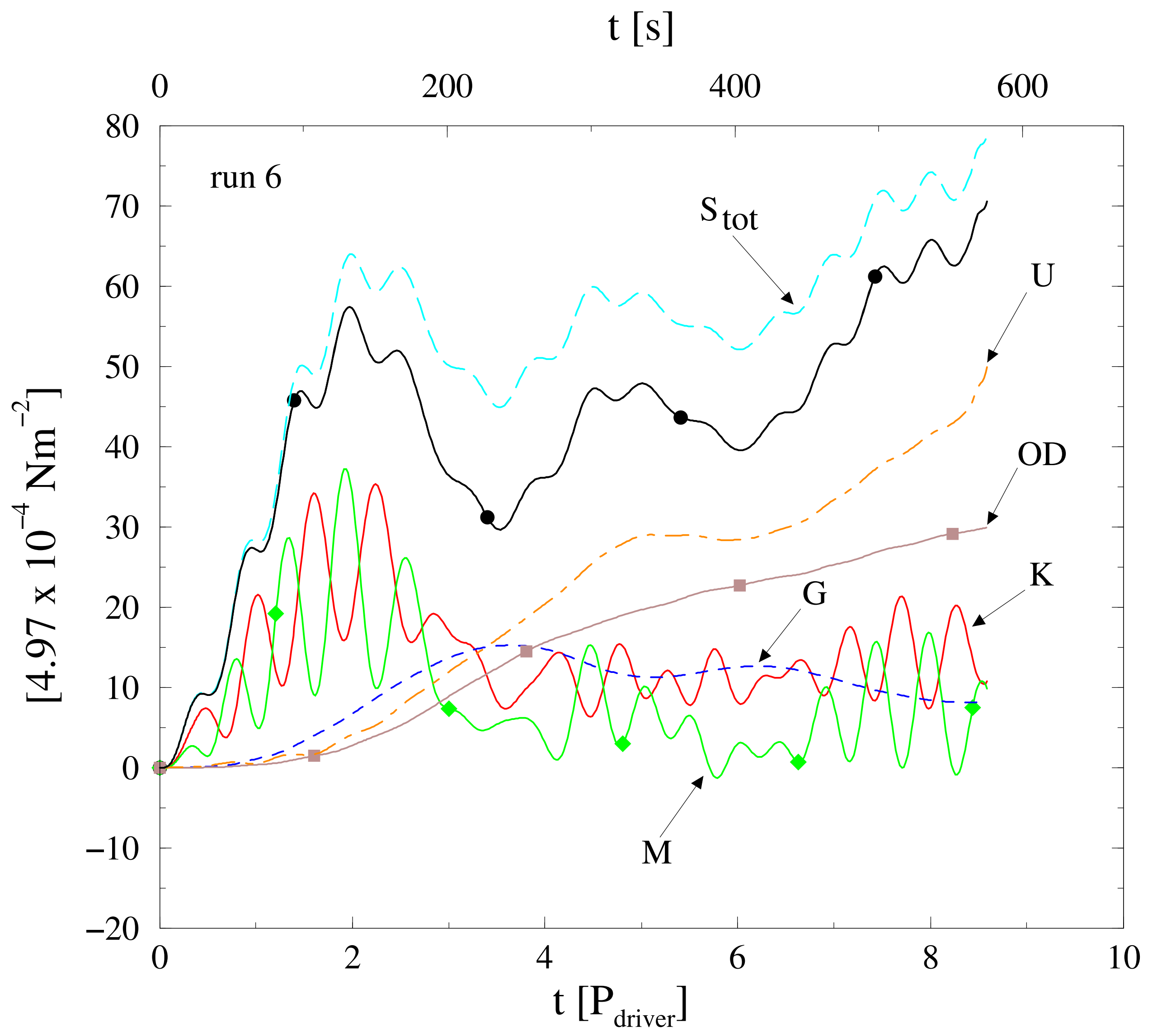
t [s]
0
200
400
600
80
70
60
50
40
30
20
10
0
−10
−20
run 6
S tot
U
OD
K
G
M
[4.97 x 10^−4 Nm^−2]
0
2
4
6
8
10
t [P driver]

Figure 2f

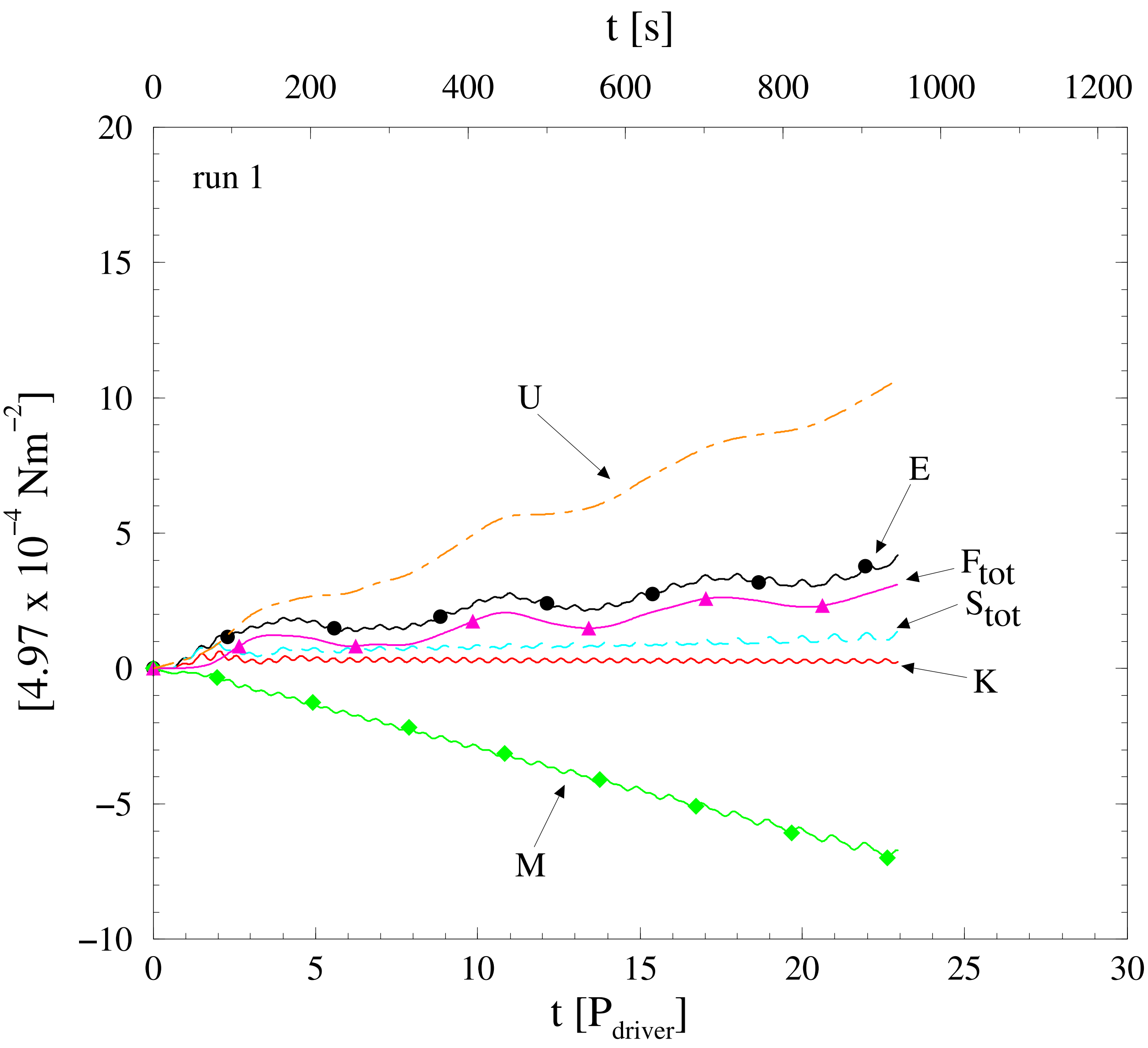
t [s]
0
200
400
600
800
1000
1200
20
15
10
5
0
−5
−10
run 1
U
E
F_{tot}
S_{tot}
K
M
$[4.97 \times 10^{-4}\ Nm^{-2}]$
0
5
10
15
20
25
30
t [P_{driver}]

Figure 3a

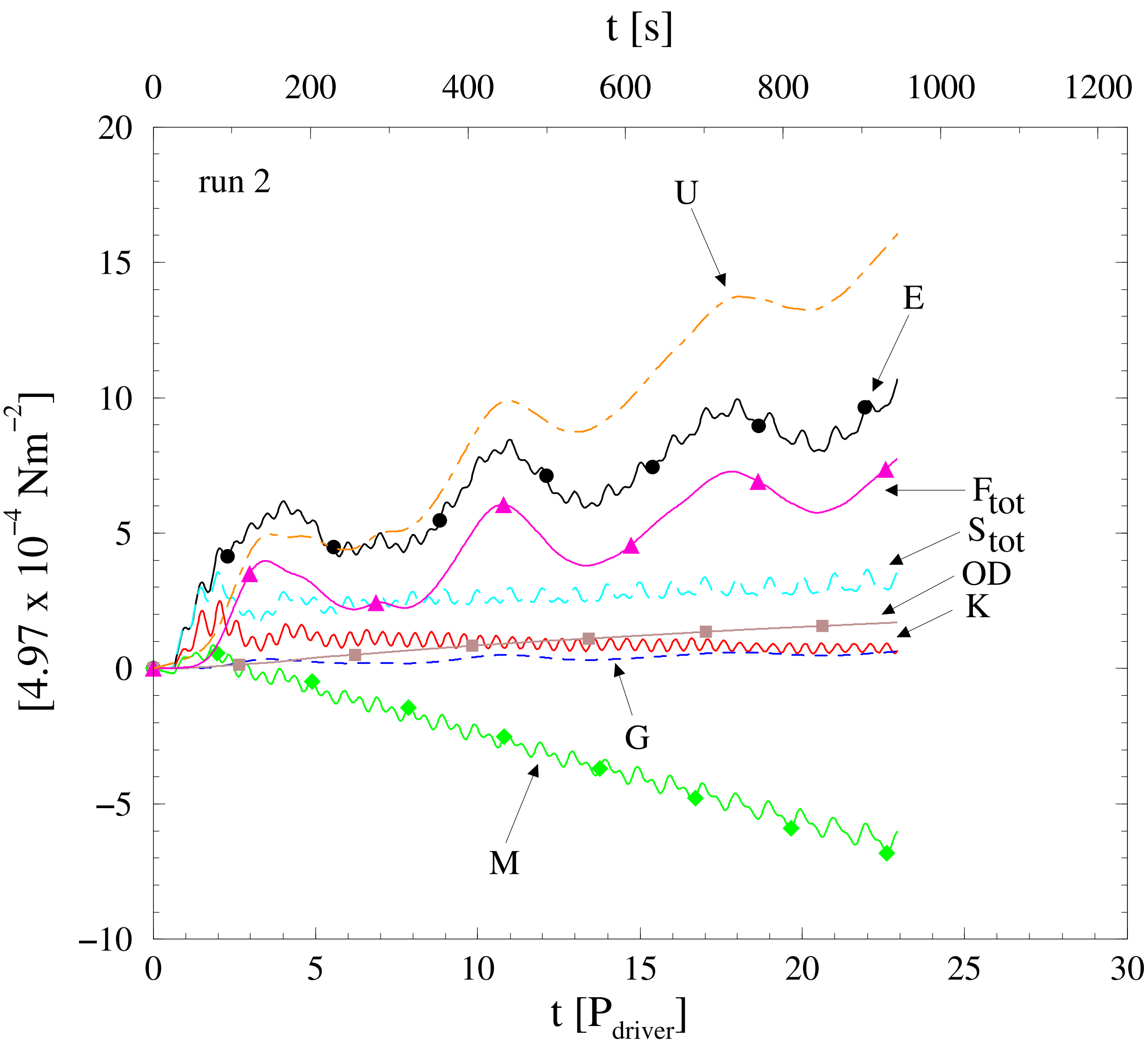

t [s]
0
200
400
600
800
1000
1200
20
15
10
5
0
–5
–10
run 2
U
E
F_{tot}
S_{tot}
OD
K
G
M
[4.97 x 10^{-4} Nm^{-2}]
0
5
10
15
20
25
30
t [P_{driver}]

Figure 3b

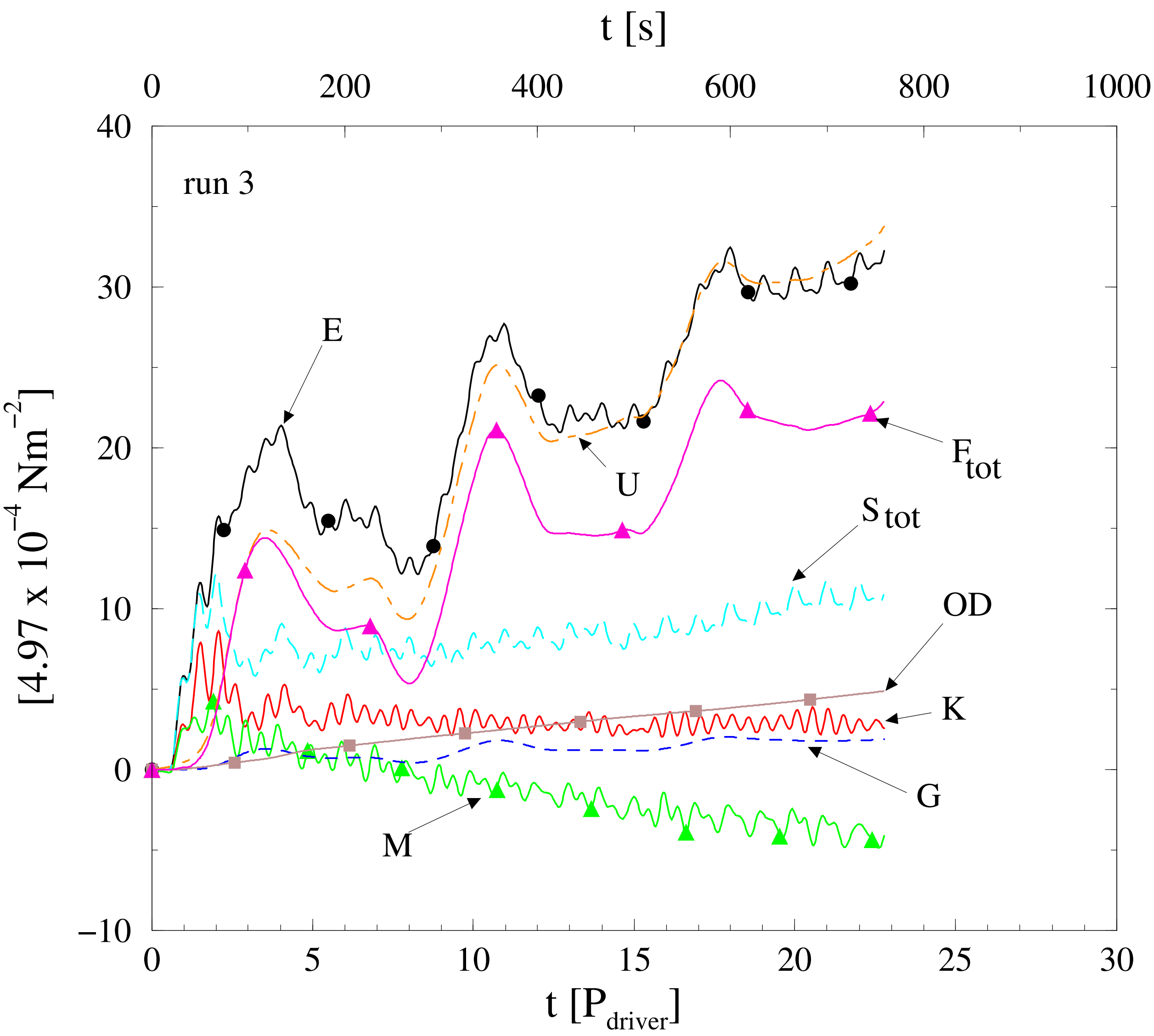

t [s]
0
200
400
600
800
1000
40
30
20
10
0
−10
run 3
E
U
F_{tot}
S_{tot}
OD
K
G
M
[4.97 x 10^{-4} Nm^{-2}]
0
5
10
15
20
25
30
t [P_{driver}]

Figure 3c

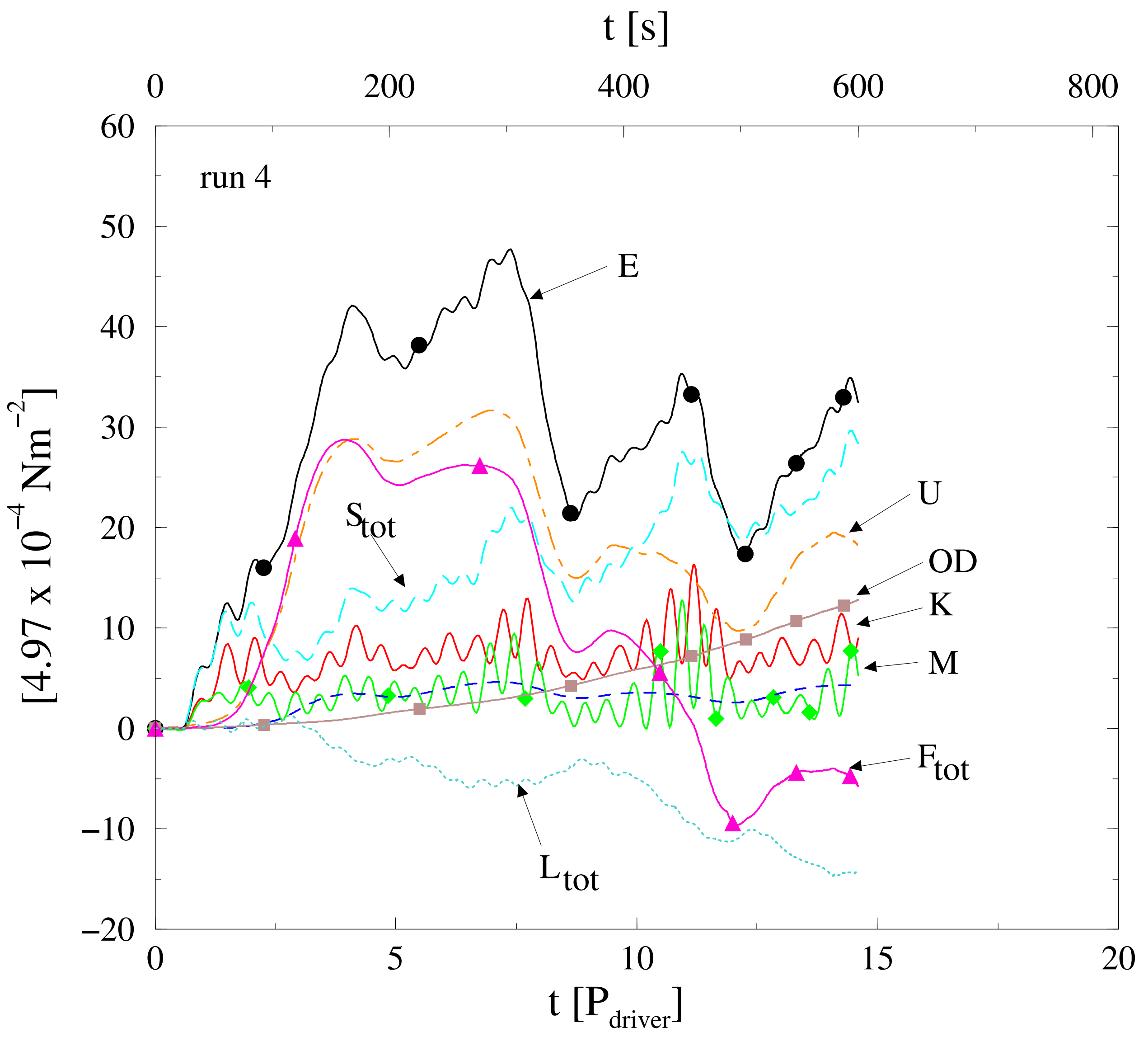

t [s]
0
200
400
600
800
60
50
40
30
20
10
0
−10
−20
[4.97 x 10^{-4} Nm^{-2}]
run 4
E
U
OD
K
M
S_{tot}
F_{tot}
L_{tot}
0
5
10
15
20
t [P_{driver}]

Figure 3d

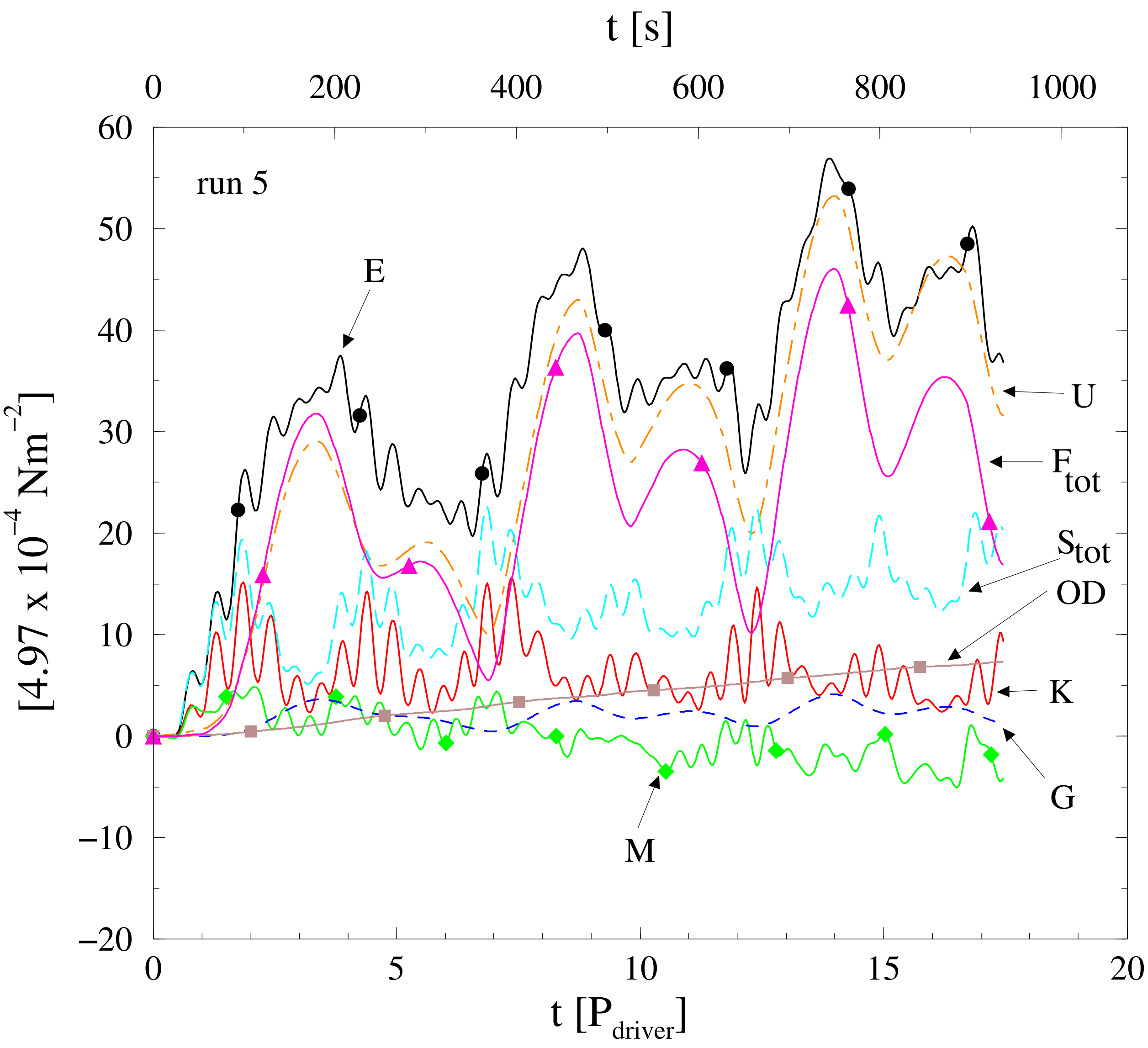
t [s]
0
200
400
600
800
1000
60
50
40
30
20
10
0
−10
−20
run 5
E
U
F
tot
S
tot
OD
K
G
M
[4.97 x 10−4 Nm−2]
0
5
10
15
20
t [P
driver]

Figure 3e

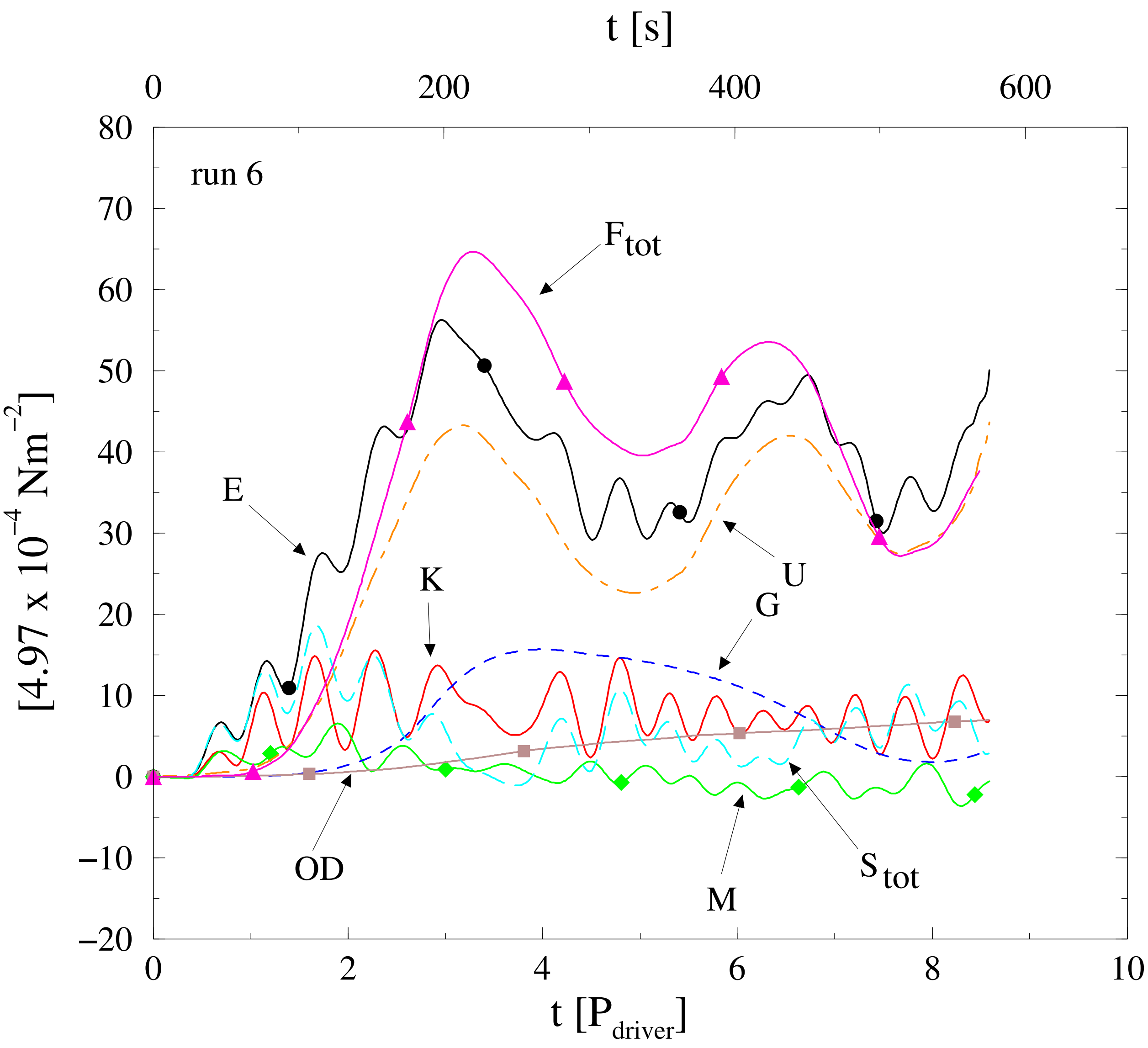

t [s]
0
200
400
600
80
70
60
50
40
30
20
10
0
−10
−20
run 6
F_{tot}
E
U
K
G
OD
M
S_{tot}
[4.97 x 10^{-4} Nm^{-2}]
0
2
4
6
8
10
t [P_{driver}]

Figure 3f

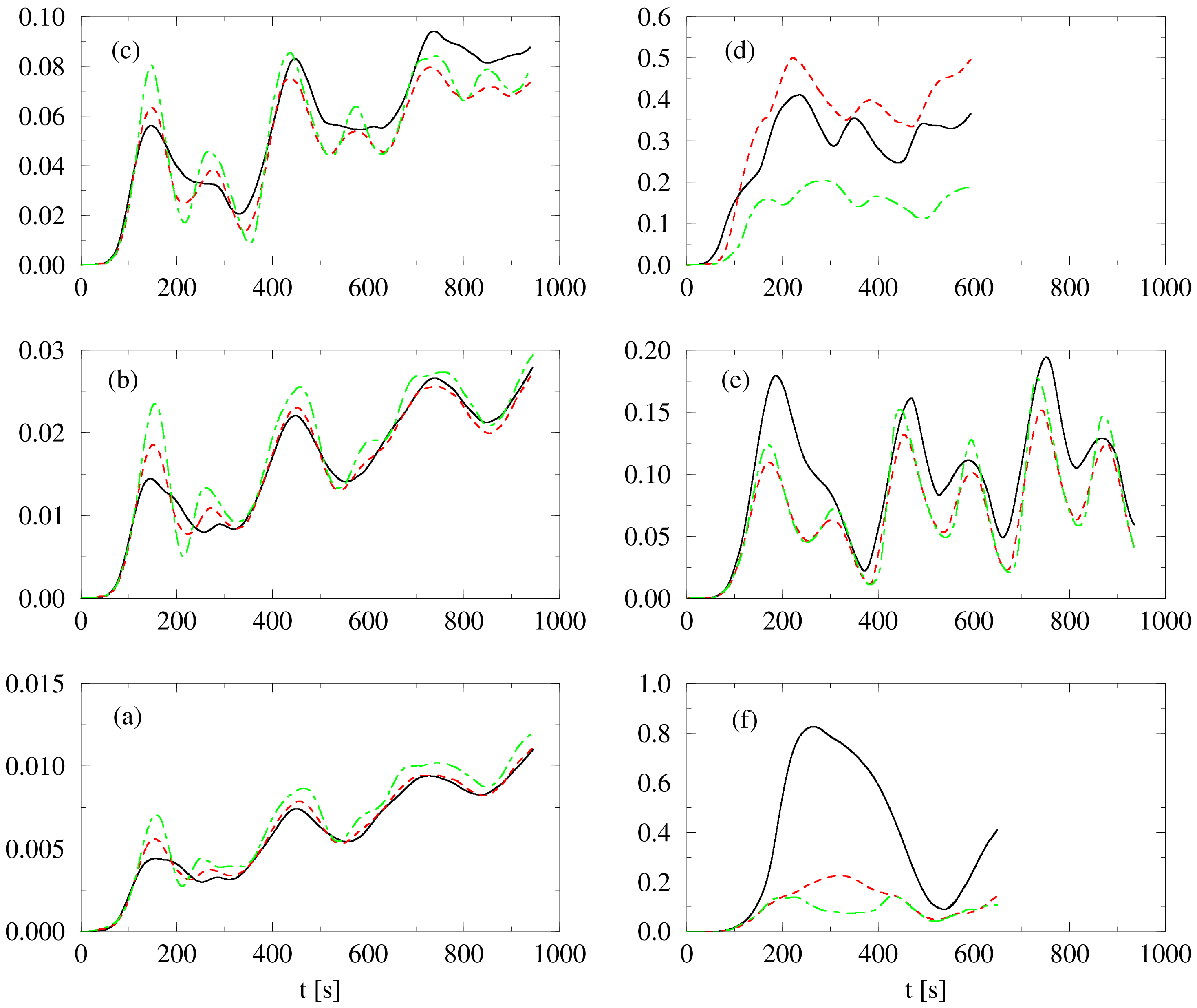

Figure 4

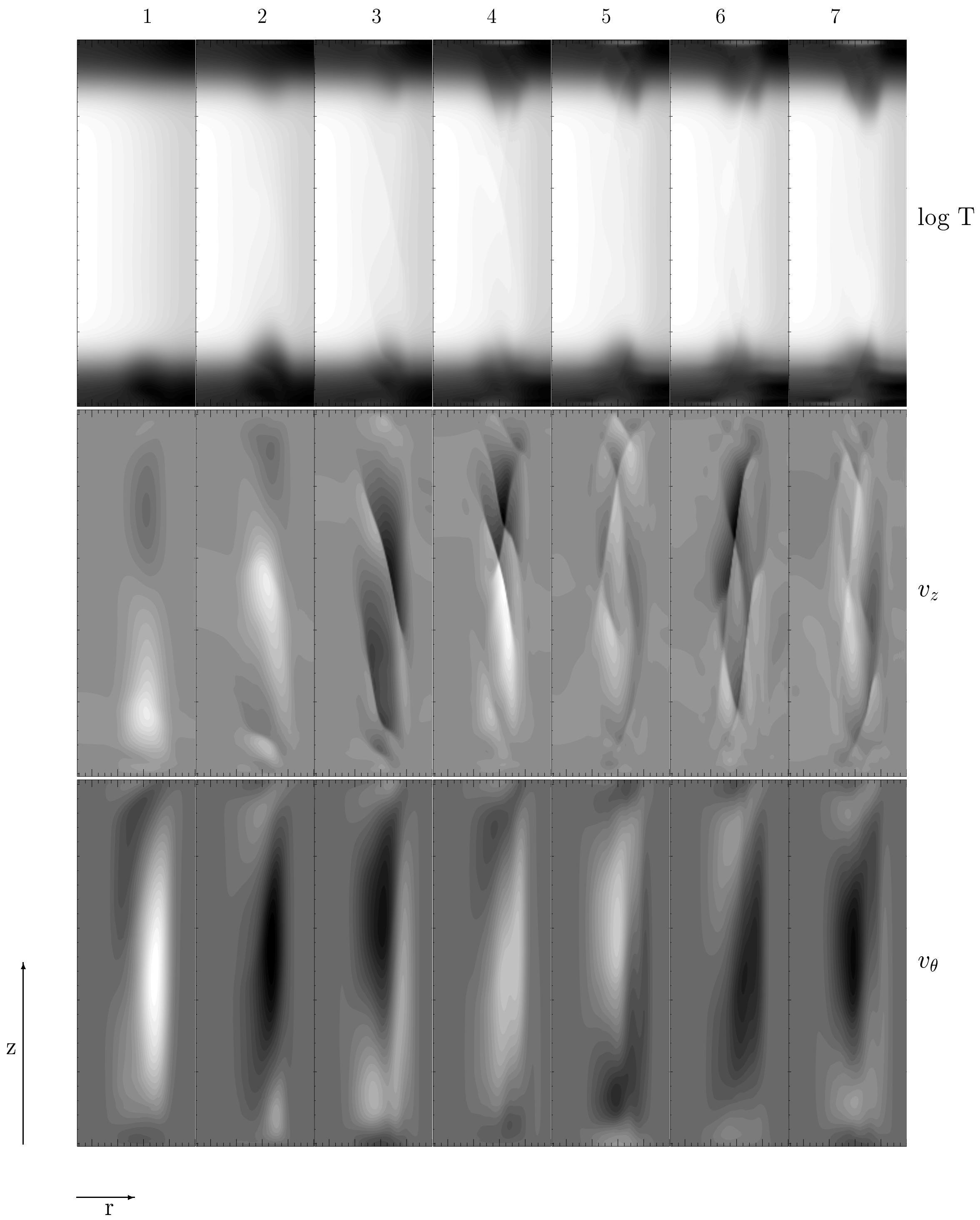

Figure 5

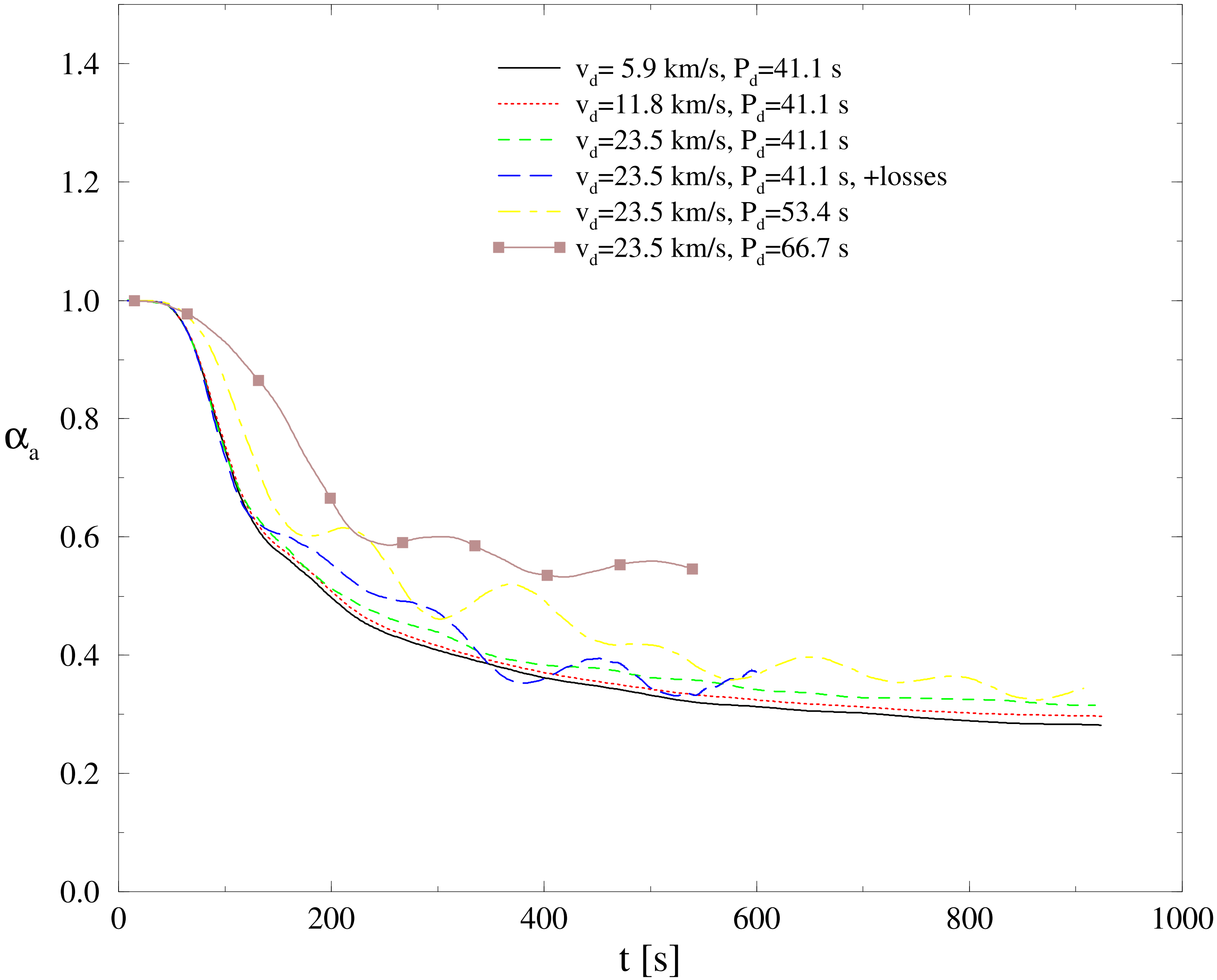

v_d= 5.9 km/s, P_d=41.1 s
v_d=11.8 km/s, P_d=41.1 s
v_d=23.5 km/s, P_d=41.1 s
v_d=23.5 km/s, P_d=41.1 s, +losses
v_d=23.5 km/s, P_d=53.4 s
v_d=23.5 km/s, P_d=66.7 s
α_a
t [s]
0.0
0.2
0.4
0.6
0.8
1.0
1.2
1.4
0
200
400
600
800
1000

Figure 6a

Figure 6b

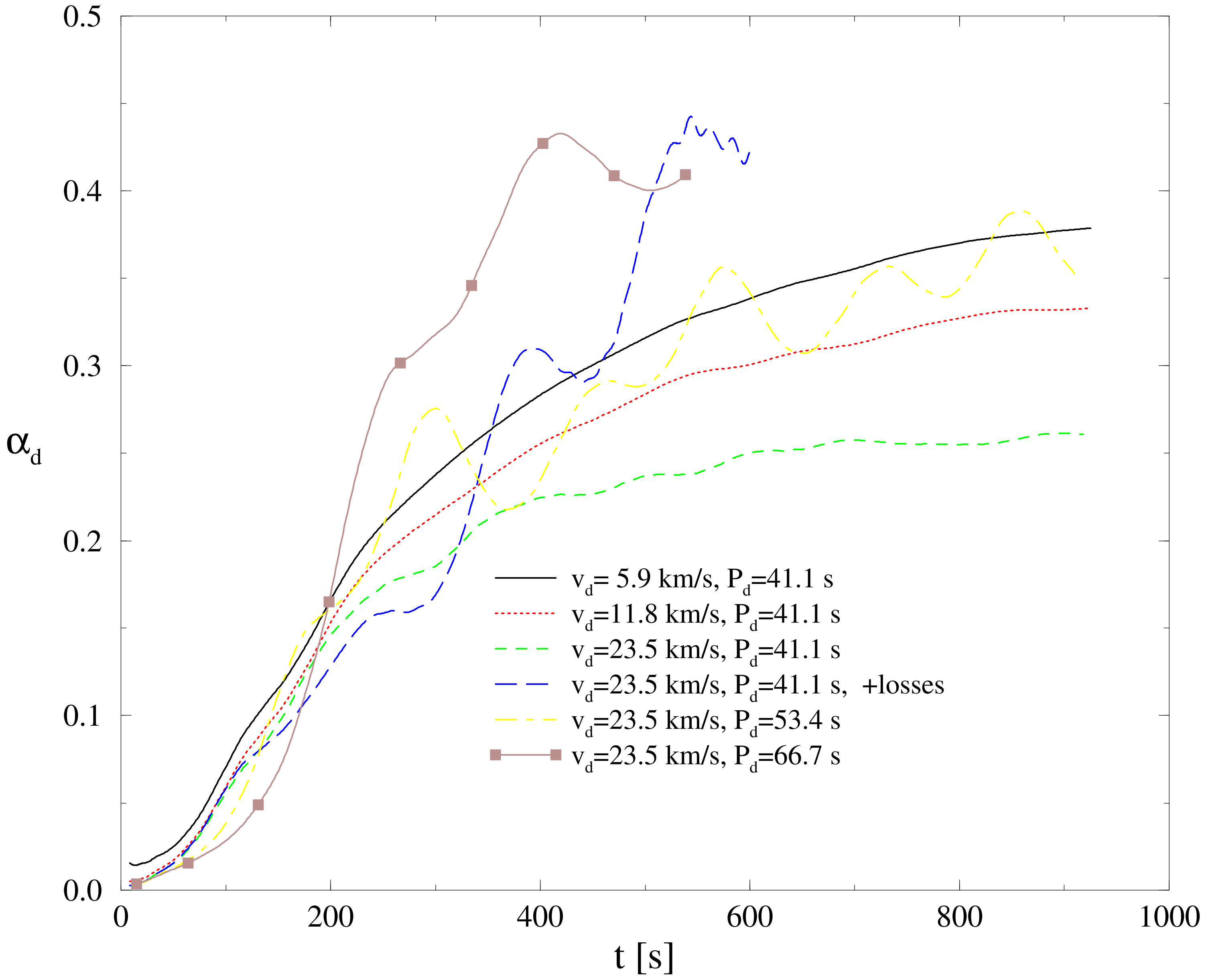

0.5
0.4
0.3
0.2
0.1
0.0
0
200
400
600
800
1000
α_d
t [s]
v_d= 5.9 km/s, P_d=41.1 s
v_d=11.8 km/s, P_d=41.1 s
v_d=23.5 km/s, P_d=41.1 s
v_d=23.5 km/s, P_d=41.1 s, +losses
v_d=23.5 km/s, P_d=53.4 s
v_d=23.5 km/s, P_d=66.7 s

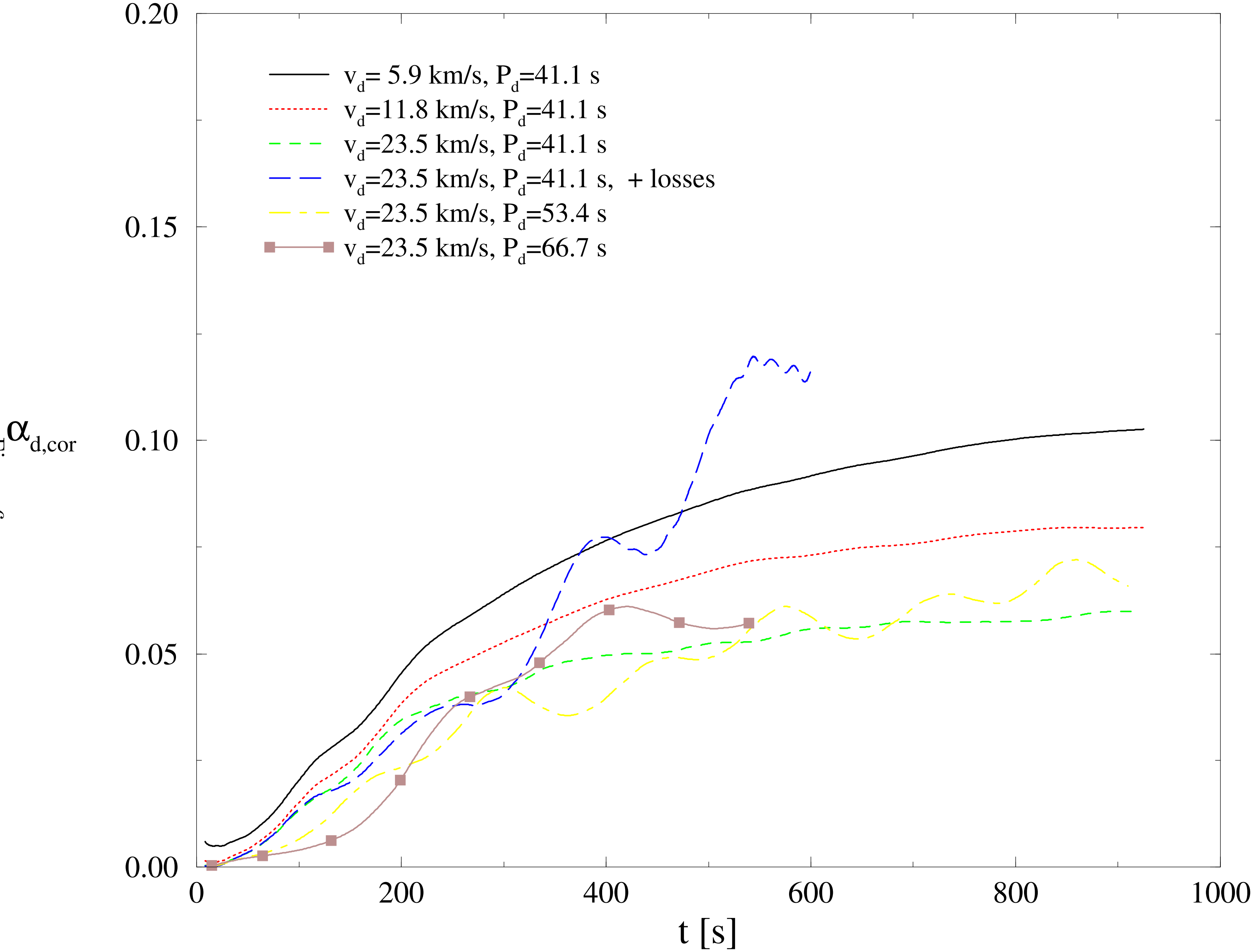

v_d= 5.9 km/s, P_d=41.1 s
v_d=11.8 km/s, P_d=41.1 s
v_d=23.5 km/s, P_d=41.1 s
v_d=23.5 km/s, P_d=41.1 s, + losses
v_d=23.5 km/s, P_d=53.4 s
v_d=23.5 km/s, P_d=66.7 s
α_d,cor
t [s]
0.00
0.05
0.10
0.15
0.20
0
200
400
600
800
1000

Figure 6c

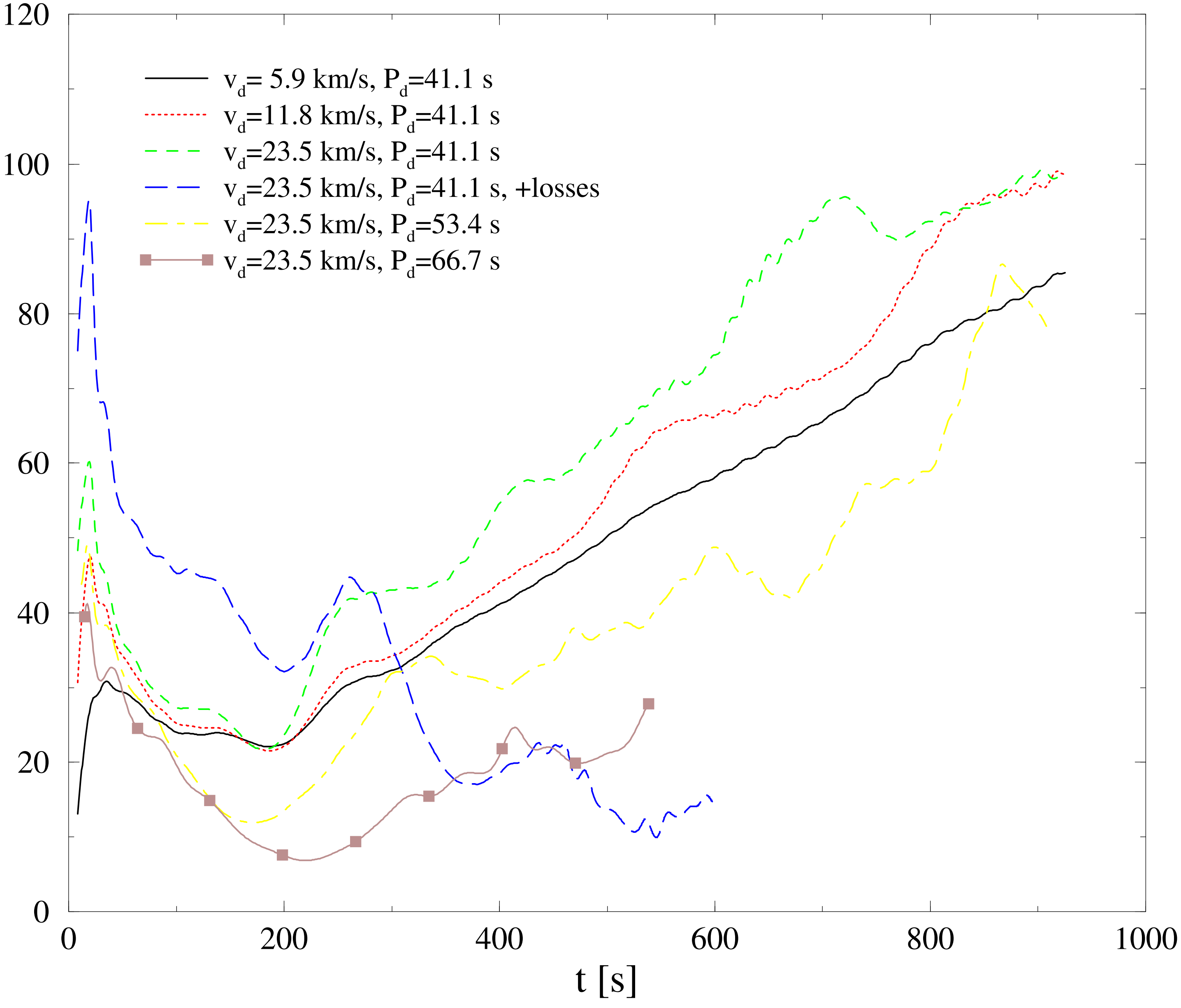

v_d= 5.9 km/s, P_d=41.1 s
v_d=11.8 km/s, P_d=41.1 s
v_d=23.5 km/s, P_d=41.1 s
v_d=23.5 km/s, P_d=41.1 s, +losses
v_d=23.5 km/s, P_d=53.4 s
v_d=23.5 km/s, P_d=66.7 s
Q
t [s]
0
20
40
60
80
100
120
200
400
600
800
1000

Figure 6d

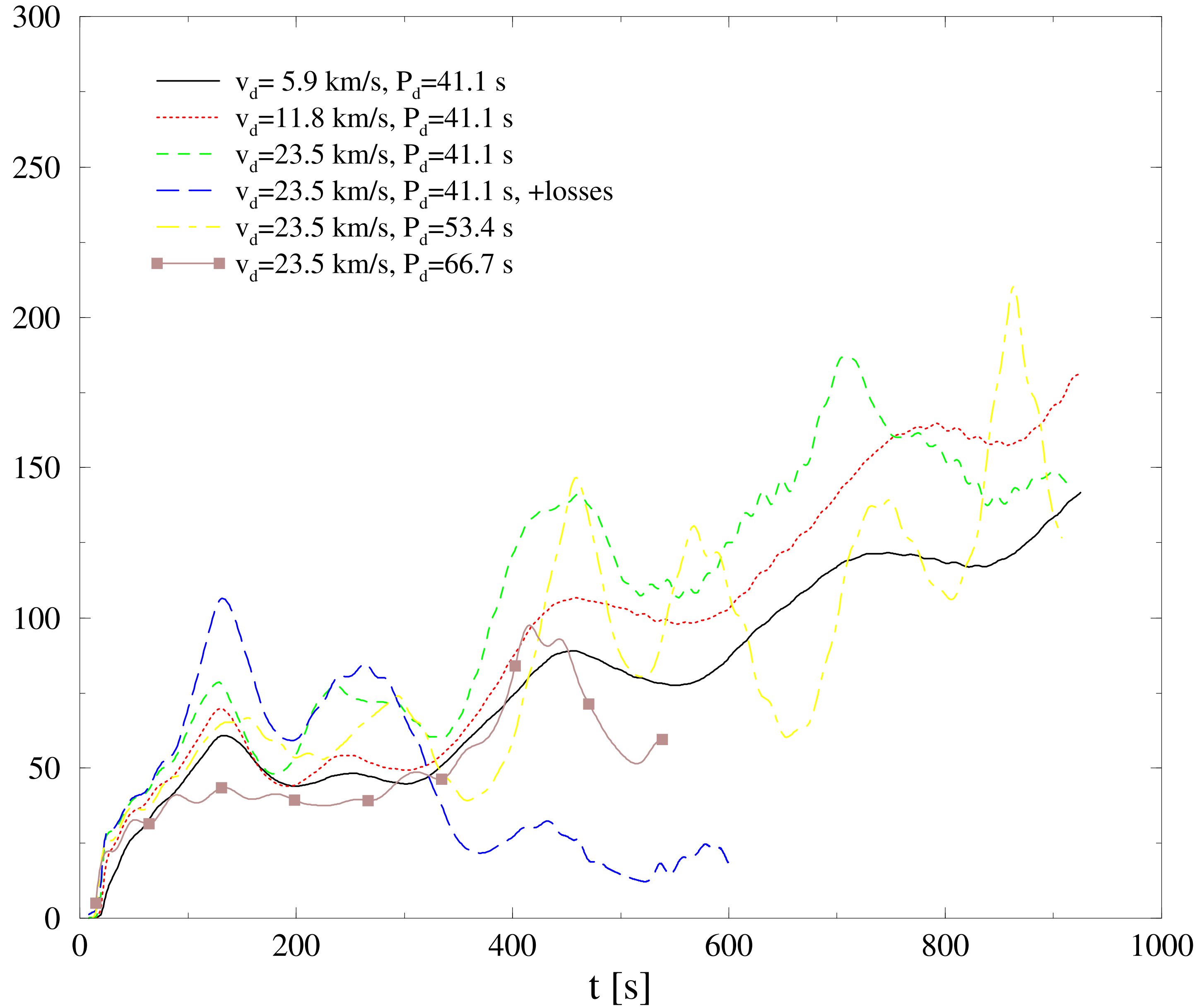

v_d= 5.9 km/s, P_d=41.1 s
v_d=11.8 km/s, P_d=41.1 s
v_d=23.5 km/s, P_d=41.1 s
v_d=23.5 km/s, P_d=41.1 s, +losses
v_d=23.5 km/s, P_d=53.4 s
v_d=23.5 km/s, P_d=66.7 s
Q_{cor}
t [s]
0
50
100
150
200
250
300
0
200
400
600
800
1000

Figure 6e

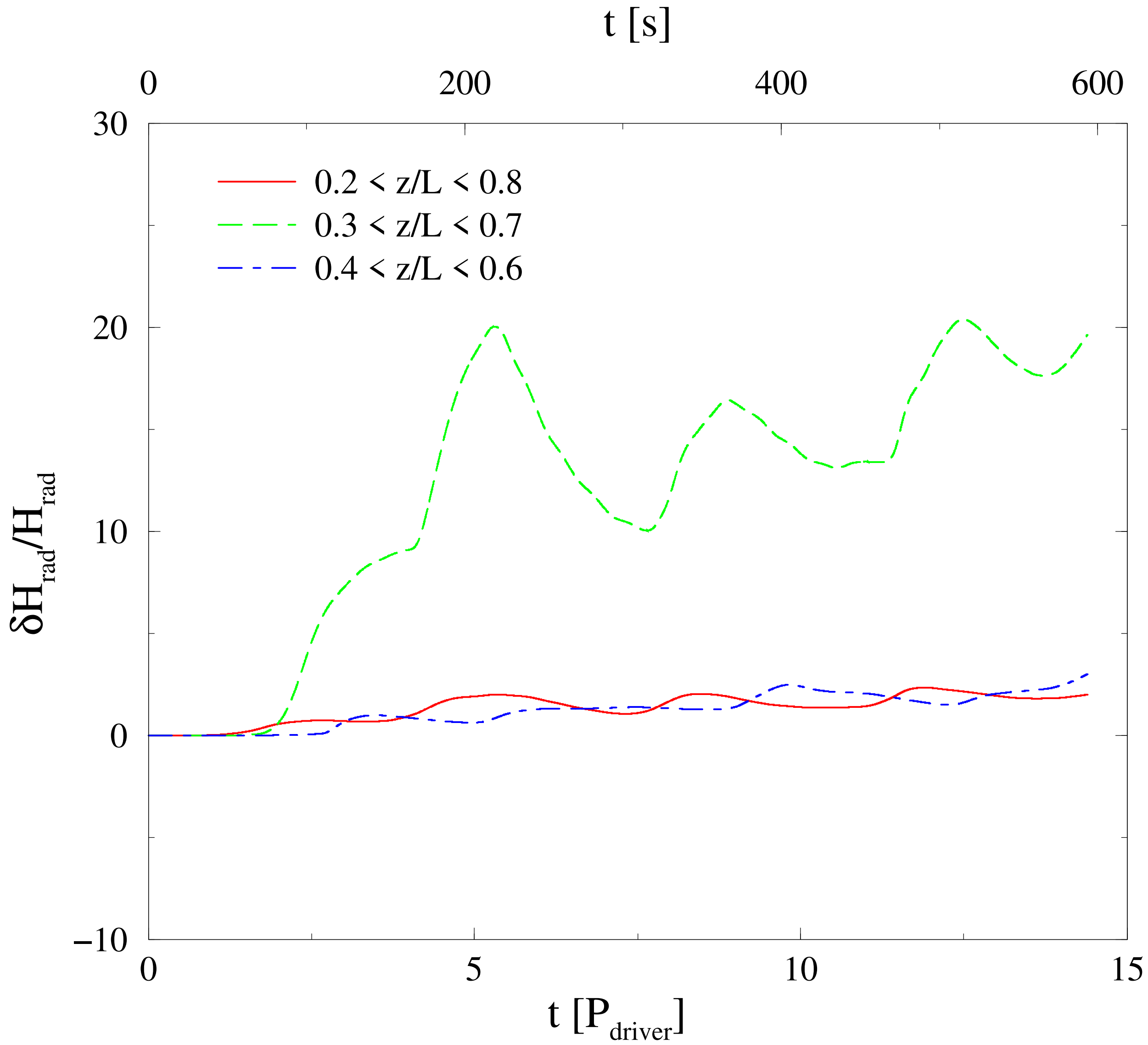
t [s]
0
200
400
600
30
20
10
0
−10
0.2 < z/L < 0.8
0.3 < z/L < 0.7
0.4 < z/L < 0.6
δH_rad/H_rad
0
5
10
15
t [P_driver]

Figure 7

Table 1. Simulation specifications

run	v_{d} [km/s]	P_{driver} [s]	duration [s]	losses	resolution [km×km]
1	5.9	41.1	942	-	10×125
2	11.8	41.1	941	-	10×125
3	23.5	41.1	935	-	10×125
4	23.5	41.1	591	+	10×62.5
5	23.5	53.4	932	-	10×125
6	23.5	66.7	647	-	10×125